J Neurophysiol 117: 2188–2208, 2017.
First published March 1, 2017; doi:10.1152/jn.00951.2016.

RESEARCH ARTICLE | *Cellular and Molecular Properties of Neurons*

Systems-based analysis of dendritic nonlinearities reveals temporal feature extraction in mouse L5 cortical neurons

Brian E. Kalmbach,[1] Richard Gray,[1] Daniel Johnston,[1] and Erik P. Cook[2]
[1]*Center for Learning and Memory, Department of Neuroscience, The University of Texas at Austin, Austin, Texas; and*
[2]*Centre for Mathematics in Bioscience and Medicine, Department of Physiology, McGill University, Montreal, Quebec, Canada*

Submitted 18 December 2016; accepted in final form 27 February 2017

Kalmbach BE, Gray R, Johnston D, Cook EP. Systems-based analysis of dendritic nonlinearities reveals temporal feature extraction in mouse L5 cortical neurons. *J Neurophysiol* 117: 2188–2208, 2017. First published March 1, 2017; doi:10.1152/jn.00951.2016.—What do dendritic nonlinearities tell a neuron about signals injected into the dendrite? Linear and nonlinear dendritic components affect how time-varying inputs are transformed into action potentials (APs), but the relative contribution of each component is unclear. We developed a novel systems-identification approach to isolate the nonlinear response of layer 5 pyramidal neuron dendrites in mouse prefrontal cortex in response to dendritic current injections. We then quantified the nonlinear component and its effect on the soma, using functional models composed of linear filters and static nonlinearities. Both noise and waveform current injections revealed linear and nonlinear components in the dendritic response. The nonlinear component consisted of fast Na^+ spikes that varied in amplitude 10-fold in a single neuron. A functional model reproduced the timing and amplitude of the dendritic spikes and revealed that they were selective to a preferred input dynamic (~4.5 ms rise time). The selectivity of the dendritic spikes became wider in the presence of additive noise, which was also predicted by the functional model. A second functional model revealed that the dendritic spikes were weakly boosted before being linearly integrated at the soma. For both our noise and waveform dendritic input, somatic APs were dependent on the somatic integration of the stimulus, followed a subset of large dendritic spikes, and were selective to the same input dynamics preferred by the dendrites. Our results suggest that the amplitude of fast dendritic spikes conveys information about high-frequency features in the dendritic input, which is then combined with low-frequency somatic integration.

NEW & NOTEWORTHY The nonlinear response of layer 5 mouse pyramidal dendrites was isolated with a novel systems-based approach. In response to dendritic current injections, the nonlinear component contained mostly fast, variable-amplitude, Na^+ spikes. A functional model accounted for the timing and amplitude of the dendritic spikes and revealed that dendritic spikes are selective to a preferred input dynamic, which was verified experimentally. Thus, fast dendritic nonlinearities behave as high-frequency feature detectors that influence somatic action potentials.

computational model; dendrite; electrophysiology; mouse; pyramidal neuron

WHAT DO DENDRITIC NONLINEARITIES tell a cortical neuron about injected signals, and how do they contribute to the action potential (AP)? The answer to this fundamental question is not as straightforward as it might seem despite many years of pioneering work (Stuart and Spruston 2015). The transformation from dendritic input to somatic AP is performed largely by the dendrites. While a component of the dendritic processing can be described by linear and frequency-dependent models (Cook et al. 2007; Hu et al. 2009; Nettleton and Spain 2000; Watanabe et al. 2014), local dendritic nonlinearities play an important role in the form of Na^+-, Ca^{2+}-, and NMDA-mediated regenerative events (Harnett et al. 2013; Larkum et al. 2009; Oviedo and Reyes 2002; Schiller et al. 1997, 2000; Smith et al. 2013; Stuart et al. 1997). In this study, we ask: what is the optimal injected input that dendrites prefer, and how does it affect AP production?

In vivo inputs arriving throughout the dendrites combine to create a time-varying signal containing multiple frequency components (Destexhe et al. 2003). This input signal is filtered by the dendrites and produces in some neurons a theta resonance (~4–12 Hz) due to the contribution of voltage-dependent channels (Cook et al. 2007; Dembrow et al. 2015; Hu et al. 2009; Kalmbach et al. 2013; Narayanan and Johnston 2007; Ulrich 2002; Vaidya and Johnston 2013). Similarly, voltage-dependent channels allow certain input patterns to more efficiently generate nonlinear dendritic spikes (Gasparini et al. 2004; Gasparini and Magee 2006; Golding and Spruston 1998; Polsky et al. 2004; Sivyer and Williams 2013; Smith et al. 2013; Stuart et al. 1997). These results suggest that dendrites extract a preferred input feature, such as a particular frequency band or temporal input structure. Thus, understanding the transformation from dendritic input to somatic output requires identifying the feature of the input to which dendritic nonlinearities are selective.

To address this, we applied a systems-based framework (Sakai 1992; Wu et al. 2006) rather than the synapse-specific and channel-based models of previous studies. We demonstrate a novel deconvolution method for isolating dendritic nonlinearities in response to arbitrary dendritic inputs. The benefit of this approach is that the contribution of complex voltage-dependent currents is reduced to a series of simple linear and nonlinear functional components. These functional compo-

Address for reprint requests and other correspondence: E. P. Cook, Dept. of Physiology, McGill Univ., 3655 Sir William Osler, Montreal, QC H3G 1Y6, Canada (e-mail: erik.cook@mcgill.ca).

nents, in turn, identify the optimal input parameters that the dendritic nonlinearities prefer.

White-noise and waveform current injections into the dendrites of mouse L5 pyramidal neurons in prefrontal cortex (PFC) revealed both linear and nonlinear components in the dendritic membrane potential. The nonlinear component consisted mainly of Na^+ spikes that varied in amplitude in single neurons by over a factor of 10, with a firing rate much higher than that of the somatic APs. These dendritic spikes were selective to a specific input dynamic (rise time of ~4.5 ms), with shorter or longer rise times producing a graded reduction in spike amplitude. Importantly, a simple functional model predicted dendritic spike timing and amplitude and reproduced the temporal selectivity of the dendritic spikes. We also observed that dendritic spikes preceded most APs and that a second functional model that linearly combined boosted dendritic spikes with the stimulus accounted for the somatic membrane potential.

This functional framework suggests that dendritic nonlinearities ensure that APs can be elicited by preferred input patterns that a linear dendrite would otherwise not detect. Thus, L5 neurons function as a two-layer neural network, with dendritic nonlinearities extracting a feature of the input and the output of this computation integrated at the soma (Das and Narayanan 2014; Larkum et al. 2009; Poirazi et al. 2003a, 2003b). These data reconcile an apparent inconsistency in the literature, that high-frequency inputs can entrain AP firing despite low-pass filtering by the dendrite-to-soma transfer function (Colgin et al. 2009; Fries 2009).

MATERIALS AND METHODS

Slice preparation. All procedures involving animals were approved by the Institutional Animal Care and Use Committee. Male C57BL/6 mice, 8–16 wk old, were anesthetized with a ketamine (100 mg/kg)-xylazine (10 mg/kg) cocktail and were perfused through the heart with ice-cold saline consisting of (in mM) 2.5 KCl, 1.25 NaH_2PO_4, 25 $NaHCO_3$, 0.5 $CaCl_2$, 7 $MgCl_2$, 7 dextrose, 205 sucrose, 1.3 ascorbate, and 3 sodium pyruvate (bubbled with 95% O_2-5% CO_2 to maintain pH at ~7.4). A vibrating tissue slicer (Vibratome 3000, Vibratome) was used to make 300-μm-thick coronal sections. Slices were held for 30 min at 35°C in a chamber filled with artificial cerebrospinal fluid (aCSF) consisting of (in mM): 125 NaCl, 2.5 KCl, 1.25 NaH_2PO_4, 25 $NaHCO_3$, 2 $CaCl_2$, 2 $MgCl_2$, 10 dextrose, and 3 sodium pyruvate (bubbled with 95% O_2-5% CO_2) and then at room temperature until the time of recording.

Whole cell recordings. Recordings were made from pyramidal tract-projecting (PT) L5 pyramidal neurons in the dorsal medial PFC ~1–2 mm anterior to bregma. The presence of membrane resonance was used to discriminate PT neurons from intratelencephalic projecting neurons (Dembrow et al. 2010, 2015; Kalmbach et al. 2013, 2015). Neurons that displayed a peak in the frequency-response curve in response to white noise $>$ 2 Hz were classified as PT neurons. Slices were placed in a submerged, heated (32–34°C) recording chamber that was continually perfused (1−2 ml/min) with bubbled aCSF containing (in mM) 125 NaCl, 3.0 KCl, 1.25 NaH_2PO_4, 25 $NaHCO_3$, 2 $CaCl_2$, 1 $MgCl_2$, 10 dextrose, 3 sodium pyruvate, 0.025 D-(−)2-amino-5-phosphonopentanoic acid, 0.002 gabazine, and 0.02 6,7-dinitroquinoxaline-2,3-dione. Slices were viewed with a Zeiss Axioskop microscope and differential interference contrast optics. Alexa 594-filled neurons were visualized with a mercury lamp and a 540-/605-nm filter set. Patch pipettes (4−8 MΩ) were pulled from borosilicate glass and wrapped with Parafilm to reduce capacitance. The pipette solution contained (in mM) 120 K gluconate, 16 KCl, 10 HEPES, 8 NaCl, 7 K_2 phosphocreatine, 0.3 Na-GTP, and 4 Mg-ATP (pH 7.3 with KOH). Neurobiotin (Vector Laboratories; 0.1%) was also included for histological processing. Alexa 594 (16 μM; Invitrogen) was included in the internal recording solution to determine the distance from the soma of the recording location upon termination of the experiment.

Data were acquired with Dagan BVC-700 (Dagan) amplifiers and custom data acquisition software written with IGOR Pro (WaveMetrics). Data were acquired at 10 kHz, filtered at 3 kHz, and digitized by an ITC-18 (InstruTech) interface. Pipette capacitance was compensated, and the bridge was balanced during each recording. Series resistance was monitored throughout each experiment and was 10–30 MΩ for somatic recordings and 15–35 MΩ for dendritic recordings. Voltages are not corrected for the liquid junction potential (estimated as ~12 mV). We verified that there was no appreciable frequency-dependent filtering of the white-noise current stimulus by the electrode.

A total of 29 dendritic recordings were made from the apical trunk and, with the exception of 2, were within 70 μm of the nexus of the apical tuft, near the L1-L2/3 border. Figure 1*A* illustrates the dendritic recording locations overlaid on a typical L5 pyramidal cell and highlights that most recordings were just proximal of the nexus, with three recordings distal to the nexus. Simultaneous soma recordings were performed in 16 of the 29 experiments.

General analysis. We used a combination of noise and waveform dendritic current injections (Fig. 1*B*) to develop four functional models of the dendritic and somatic membrane responses (Fig. 1*C*). Although the mathematical details of each functional model are described below in MATERIALS AND METHODS, for clarity we also include each model's structure in RESULTS. The analysis and modeling were performed in MATLAB R2014b. Error bars and variability are reported as SE unless otherwise noted. Statistical analyses were performed with the MATLAB ttest and corr (Pearson's correlation, *R*) functions.

Stimulus and TTX conditions. All 29 dendritic recordings were performed with a stimulus current injected (referred to as I_{in}) through the dendritic recording pipette for 1–2 min. Every experiment included a large, zero-mean, Gaussian-distributed white-noise input condition (Fig. 1*B*, *top*). For the large noise the variance was set to be above the threshold that produced somatic APs. In 15 experiments we included the small-noise input condition, which was subthreshold with no somatic APs. A different random seed was used for each experiment, but for a given neuron the large- and small-amplitude noise injections had the same seed and only the variance was different.

In 14 experiments we also included two other dendritic current injections. First, a sequence of waveforms was injected (Fig. 1*B*, *middle*), which we refer to as signal. For this stimulus different signal waveforms were injected every 50 ms, where the shape of each waveform was determined by our initial set of experiments using the noise stimulus (see below). Second, a signal+noise input condition (Fig. 1*B*, *bottom*) was also used in which the same waveforms were added to the 50% amplitude large-noise condition.

For the 16 of the 29 experiments in which we simultaneously recorded the soma potential, 11 soma recordings were performed during the small-noise conditions and 5 soma recordings were performed during the waveforms (signal only and signal+noise). Details of how the signal-only and signal+noise waveforms were constructed are described below in MATERIALS AND METHODS. In four experiments, TTX was either bath applied or puffed on the dendritic recording site after recordings were performed in the normal external solution. Before and during local TTX application at the dendritic recording site, somatic APs were elicited by 3-ms step current injections delivered through the somatic recoding electrode.

Preprocessing of electrophysiological recordings. Except for a single experiment, the same input conditions were alternately presented for multiple sweeps (range 2–6, median = 5 sweeps per condition). Individual sweeps of the dendritic and soma membrane potential were detrended by using a second-order polynomial to

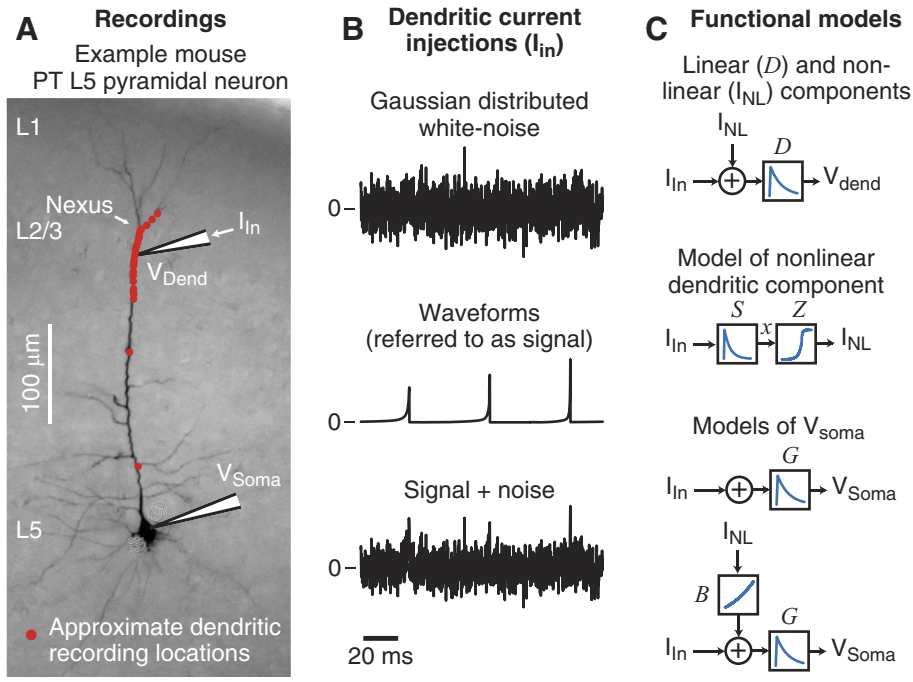

Fig. 1. Summary of recording locations, dendritic stimuli and functional models. *A*: typical mouse pyramidal tract-projecting (PT) L5 neuron that is representative of the neurons recorded in these experiments. Current stimuli (I_{in}) were injected through the dendritic electrode while the dendritic potential (V_{dend}) was measured. In 16 of 29 experiments the somatic potential (V_{soma}) was also simultaneously recorded. The approximate recording location (red dots) of each experiment is overlaid. Most dendritic recordings were just proximal to the nexus of the main apical dendrite, with 3 recordings distal to the nexus. *B*: short examples of the 3 types of current stimuli injected into the dendrites. *Top:* Gaussian-distributed white noise. *Middle:* a randomized sequence of 9 different waveforms (referred to as signals) at 50-ms intervals, whose shapes were based on the initial characterization of the dendritic nonlinearities. *Bottom:* a combination of 50%-amplitude white noise and the waveforms (referred to as signal+noise). Stimulus injections lasted 1–2 min. See MATERIALS AND METHODS for details regarding stimulus generation. *C*: summary of the functional models used to analyze the data. *Top:* the dendritic potential was described by a linear filter (*D*) convolved with the current stimulus (I_{in}) plus a current that represented the contribution of the dendritic nonlinearities (I_{NL}). *Middle:* the dendritic nonlinearity (I_{NL}) was modeled as the convolution of the dendritic input (I_{in}) with a linear spike filter (*S*), with the output of the filter (*x*) passed through a static, sigmoidal-shaped, nonlinearity (*Z*). *Bottom:* a linear filter (*G*) convolved with the dendritic input described the somatic potential. A second model added in the dendritic nonlinearity (I_{NL}) that was first slightly boosted by a quadratic function (*B*). See MATERIALS AND METHODS for details of the functional models.

remove small DC drifts during the long 1- to 2-min recording. Individual sweeps were then averaged together for most analyses in order to reduce experimental noise. However, single sweeps were analyzed individually when examining the repeatability of nonlinear current I_{NL} and the relationship between individual dendritic spikes and individual somatic APs.

Estimation of linear component of dendritic response. As shown in Fig. 1*C*, *top*, we first estimated the impulse response function of the linear filter (*D*) that best accounted for the recorded dendritic potential, V_{dend}, with

$$V_{dend} = D * I_{in} + k \quad (1)$$

where I_{in} is the current injected at the dendritic electrode, k is a constant, and * is the convolution operator. Preliminary analysis showed that most of the power in V_{dend} was below 1 kHz; thus we downsampled at 2 kHz, resulting in 120,000 data points for a 1-min recording sweep (or 240,000 data points for a 2-min recording sweep). Filter *D* was assumed to have an impulse response function $<$ 250 ms (or 500 elements at the 2 kHz sample rate). We represented the convolution in *Eq. 1* as the matrix multiplication

$$\mathbf{AD} = \mathbf{V}_{dend} \quad (2)$$

where $\mathbf{A}$ is an $N \times L_D + 1$ design matrix, L_D is the length of filter *D* (500 samples), and $\mathbf{D}$ and $\mathbf{V}_{dend}$ are column vectors of length $L_D + 1$ and N, respectively. Note that $\mathbf{D}$ includes the constant term k and that N is the number of data points = 120,000 (or 240,000). *Equation 2* is an overdetermined system of linear equations and was solved for $\mathbf{D}$ with MATLAB's linear regression function. The estimated dendritic potential, $\hat{V}_{dend}$, was then computed with *Eq. 1*.

The goodness of fit of $\hat{V}_{dend}$ was quantified with the R^2 metric (referred to here as variance accounted for or VAF). Because the number of data points was much larger than the number of free parameters in *D*, the bias in our reported VAF was estimated with an adjusted R^2 (Zar 1999) and found to be ~0.1%. Linear filters (*D*) were estimated separately for each cell and input condition and, on average, were found to be very similar across conditions. For display purposes, $\hat{V}_{dend}$ was upsampled back to the original 10 kHz sampling rate with Fourier interpolation.

Estimation of the nonlinear (I_{NL}) component of the dendritic response. The error in the linear fit of the dendritic membrane potential

$$V_{error} = V_{dend} - \hat{V}_{dend} \quad (3)$$

was assumed to be due to a nonlinearity in the dendritic response that was not captured by the linear filter (*D*). We observed that V_{error} was near zero most of the time. When errors occurred, however, they were mostly transient, positive, deflections that decayed with a timescale similar to the shape of the filter (*D*). This suggested that the nonlinearity in the dendritic response could be modeled as current impulses located at the input to the linear filter (*D*). Thus, we deconvolved V_{error} in *Eq. 3* back across the linear filter (*D*), which transformed V_{error} into the nonlinear current I_{NL} (Fig. 1*C*, *top*), such that

$$V_{error} = I_{NL} * D \quad (4)$$

If I_{NL} is computable, which is not always guaranteed and can depend on the amount of experimental noise present in the dendritic recording V_{dend}, then from *Eqs. 1*, *3*, and *4*, the dendritic potential is fully described by

$$V_{\text{dend}} = \hat{V}_{\text{dend}} + V_{\text{error}} = D * I_{\text{in}} + k + D * I_{\text{NL}} = D * (I_{\text{in}} + I_{\text{NL}}) + k \quad (5)$$

To estimate I_{NL}, we expressed the convolution in *Eq. 4* in matrix form as

$$\mathbf{B}\mathbf{I}_{\mathbf{NL}} = \mathbf{V}_{\mathbf{error}} \quad (6)$$

where $\mathbf{B}$ is a $M \times M + L_D$ design matrix constructed from D and $\mathbf{I}_{\mathbf{NL}}$ and $\mathbf{V}_{\mathbf{error}}$ are column vectors of length $M + L_D$ and M, respectively. *Equation 6* represents an underdetermined system of linear equations, and we solved for $\mathbf{I}_{\mathbf{NL}}$ with the MATLAB function mldivide. Because of the computational limits for inverting the large matrix $\mathbf{B}$, we solved for $\mathbf{I}_{\mathbf{NL}}$ in overlapping 6-s blocks (M = 12,000). Note that using the 2 kHz sampling rate had the beneficial effect of reducing high-frequency noise, which could adversely affect the deconvolution process. However, this tended to smooth the nonlinear spikes contained in I_{NL}.

Estimating I_{NL} using deconvolution worked well with our dendritic recordings and only failed on ~2% of individual recording sweeps. Inspection showed that these recording sweeps contained large amounts of experimental noise and were eliminated from further analysis. We verified all estimates of I_{NL} by recomputing V_{dend} with *Eq. 5* and showing that it matched the recorded dendritic potential. Finally, for display purposes I_{NL} was upsampled back to the original 10 kHz time base with Fourier interpolation.

Reliability of I_{NL} to repeated stimulus sweeps. Because the deconvolution of V_{error} enhanced high-frequency experimental noise in our dendritic recordings, we examined the reliability of I_{NL} to repeated presentation of identical large-noise stimulus sweeps. We hypothesized that if I_{NL} was driven by the stimulus and not the experimental noise, then it would be similar for every identical stimulus sweep. We quantified this reproducibility by computing the Pearson's correlation between individual sweeps of I_{NL} that were first convolved by a Gaussian. The standard deviation of the Gaussian represented the temporal resolution under which the correlation was computed. For example, as the temporal resolution becomes larger, the correlation becomes less dependent on the exact timing of spikes in I_{NL}. At a temporal resolution of ~0.5 ms, the average correlation between I_{NL} sweeps plateaued at a relatively high value (~0.9).

Noise floor and identifying individual current spikes in I_{NL}. We identified individual current spikes contained in I_{NL} based primarily on amplitude. Thus, we first set a criterion for the minimum spike amplitude (referred to as the noise floor, dashed line in most plots of I_{NL}). For each experiment, we estimated the noise floor as the three-standard deviation level (99.7%) of the negative amplitude distribution of I_{NL}. As shown by the population amplitude distribution (see Fig. 3*B* below), I_{NL} was positively skewed above the average noise floor. In addition to the minimum spike amplitude (i.e., noise floor), spikes were also isolated based on a width at half-height $<$ 2.5 ms.

Spike-triggered average of I_{NL}. To compute the spike-triggered averages (STAs) of I_{NL}, we selected well-isolated spikes that had amplitudes $>$ 1.5 $\times$ noise floor and that did not occur within 10 ms of a preceding dendritic spike or somatic AP. This selection process resulted in 23,820 identified dendrite spikes used to compute the STAs and ensured that all spikes were well isolated, unlikely to be due to noise, and not linked to a dendritic burst or back-propagating somatic APs.

Estimation of the cascade model of I_{NL}. We modeled I_{NL} as a function of the stimulus, using a standard cascade model of a linear filter followed by a static nonlinearity (Fig. 1*C*, *middle*). This type of functional model (usually referred to as an LN model) and its many variants have a long track record of modeling the spike activity of neurons (Hunter and Korenberg 1986; Sakai 1992; Wu et al. 2006).

In this model, I_{NL} was modeled as a linear "spike" filter (S) convolved with the stimulus, I_{in}. The output of the spike filter (x) was then mapped onto a static nonlinearity (Z) that transformed how well the stimulus matched the spike filter into a graded nonlinear current spike. Based on the shape of the stimulus STA of I_{NL}, the spike filter's impulse response function was set be 200 ms long and parametrically modeled with Gaussian and exponential functions. The Gaussian part, H, was used to model the rise of the filter S (first 0.5 ms), and the exponential part, E, described the decay of the filter such that

$$S(t) = \begin{cases} H(t) \text{ for } t < 0.5 \text{ ms} \\ E(t) \text{ for } t \geq 0.5 \text{ ms} \end{cases} \quad (7)$$

where

$$H(t) = Ae^{-\left(\frac{(t-\mu)}{\sigma}\right)^2} \quad (8)$$

$$E(t) = B_1 e^{\frac{-(t-0.5)}{\tau_1}} + B_2 e^{\frac{-(t-0.5)}{\tau_2}} + B_3 e^{\frac{-(t-0.5)}{\tau_3}} + c \quad (9)$$

Thus, the spike filter (S) had 10 free parameters.

The static nonlinearity (Z) was modeled as two generalized sigmoidal functions based on our inspection of the relationship between the output (x) of the spike filter (S) and the actual spike amplitudes. Thus, we used two general sigmoid functions to describe the initial slow amplitude rise (Q_1) and faster amplitude saturation (Q_2) of the dendritic spikes:

$$Z(x) = \begin{cases} Q_1(x) \text{ for } x < x0 \\ Q_2(x) \text{ for } x \geq x0 \end{cases} \quad (10)$$

where

$$Q_i(x) = \frac{\beta}{\left(1 + e^{-b_i (x-x0)}\right)^{1/v}} \text{ for } i = 1, 2 \quad (11)$$

with 5 free parameters in the static nonlinearity (Z).

The most important aspect of the optimization was accounting for the temporal jitter between actual and model I_{NL} spikes. Careful inspection of the relative alignment of the stimulus and I_{NL} spike STAs revealed that the actual spike peaks varied in latency depending on their amplitude. Small dendritic current spikes in I_{NL} peaked immediately after the stimulus, while large dendritic spikes required an additional 0.5 ms to reach their peak amplitudes. Thus, we allowed the model spikes to vary in their alignment with the data, within a range of 0.7 ms before to 0.2 ms after an actual dendritic spike. This was accomplished by sliding a 1-ms-wide "max filter" across the output of the static nonlinearity (Z) such that

$$\text{model } I_{NL} = \overset{\max}{W}\{Z(S * I\text{in})\} \quad (12)$$

where W is the 1-ms max window. As this produced model spikes resembling 1-ms square pulses, for display purposes model spikes greater than or equal to the noise floor were replaced with a 1-ms-wide Hann window centered on the square spike, while model I_{NL} values less than the noise floor were set to zero.

We optimized the model (*Eq. 12*) separately for each cell. To speed up the optimization, we only fit the model to the isolated dendritic spike times and peak amplitudes that were greater than or equal to the noise floor. We used the MATLAB function lsqcurvefit to optimize the model parameters. Note that since β in *Eq. 11* is linear within the parameters, it was solved for with linear regression on every optimization step. Initial starting values for the parameters were based on the stimulus STA of I_{NL}. Because the amplitude of the model's dendritic spikes was an important feature of the model, the saturating nonlinearity (Z) precluded the use of a more efficient optimization approach (Paninski 2004).

The number of spikes typically available in a single experiment was relatively small (~1,500 on average); thus we used twofold cross-validation to assess the goodness of fit of the model. The validated VAF of the model was based on fitting the model to half the data and testing the goodness of fit on the other half. Overall, the

model did relatively well, capturing the spike timing and amplitude with a median cross-validated VAF = 85%. Note that we also validated the model using the ~98% of the data where I_{NL} was below the noise floor and not used for the optimization. In this case, the model false alarm rate was very low (reported in RESULTS). Although we do not claim that our model of the dendritic nonlinearity (I_{NL}) represents a global best fit, it was remarkably good at mimicking the dendritic spike timing and amplitude in the data, as well as predicting the selectivity profile in response to waveform stimuli injected into the dendrite.

Temporal selectivity of I_{NL}. To measure the temporal selectivity of I_{NL}, we injected the signal-only and signal+noise waveforms (Fig. 1*B*) into the dendrites. Each stimulus contained a series of 9 stretched or compressed versions of the average dendritic STA of I_{NL} estimated from the first 10 large-noise experiments. Signal waveforms were presented every 50 ms in a random order. All signal waveforms were normalized to their sum of squared values in order for each signal to have equal energy (Lathi and Ding 2010). For the signal+noise condition, the same signals were added to the 50%-reduced large white-noise input. The amplitude of the injected signals was set to be at threshold in order to produce the occasional somatic AP for the preferred signal rise time.

To construct selectivity curves, we computed the peak of the average I_{NL} that followed each of the nine signal waveforms and plotted this average peak current vs. the log of the 10–90% rise time of the signal waveforms. The selectivity profile was then described by fitting a Gaussian function to this data with

$$\text{peak } I_{NL} = Ae^{-\left(\frac{(r-\mu)}{\sigma}\right)^2} + C \quad (13)$$

where r is 10–90% rise time of the input signal, C is a constant, and the selectivity parameters of interest are the preferred rise time (μ) and selectivity width (σ).

We fit the same cascade model described above to the model I_{NL} in response to the signal-only and signal+noise dendritic inputs. The model used the same spike filter (S) estimated from the large-noise condition, but we refit the static nonlinearity (Z). This was because during the signal-only and signal+noise conditions the amplitudes of I_{NL} spikes were ~50 and 75% smaller, respectively, compared with spikes in the large-noise condition. Using the model I_{NL} response to the signal-only and signal+noise conditions, we fit the same Gaussian (*Eq. 13*) to extract the model's selectivity and compared these to the selectivity parameters observed for each cell.

Somatic integration of dendritic spikes. To measure the effect that the dendritic spikes contained in I_{NL} had on the response at the soma, we performed 16 experiments with simultaneous dendritic and soma electrodes. Large-amplitude white noise was injected through the dendritic electrode, and I_{NL} was computed as described above. For all analysis involving somatic responses we only used single recording sweeps, in order to precisely capture the relative timing between the dendritic spike and somatic AP.

As shown in Fig. 1*C*, *bottom*, we modeled the response at the soma, V_{soma}, using two functional models. In the first, we estimated a soma linear filter, G, such that

$$V_{soma} = G * I_{in} + k \quad (14)$$

We estimated the soma linear filter (G) with the same methods as those for estimating the dendritic linear filter (D).

To investigate the contribution of I_{NL} to the soma response, we added a boosted version of I_{NL} to the noise stimulus such that

$$V_{soma} = G * [I_{in} + B(I_{NL})] + k \quad (15)$$

where $B(x) = ax + bx^2$ and accounted for additional nonlinear contributions to the somatic potential. Thus, the boosting of the nonlinear current in *Eq. 15* captured the additional nonlinearities in the neuron not measured at the dendritic electrode. Note, however, that the boost did not change the dynamics of the dendritic nonlinearity but only scaled its amplitude. The linear filter G was essentially the same whether it was estimated using only the noise stimulus (*Eq. 14*) or also included I_{NL} (*Eq. 15*).

Latency of individual somatic APs. We isolated 3,241 individual somatic APs. The latency of the soma AP was measured from the start of the nearest dendritic spike to the start of the AP. Because of the noise floor, it was difficult to estimate the start of the dendritic spike from a threshold applied to the derivative of I_{NL}. Therefore, we estimated the start of the dendritic spike by projecting a line down from the maximal slope of its rising phase. This line had the same slope as the maximal slope, and where it crossed zero was recorded as the start of the dendritic spike. Inspection of individual dendritic spikes suggested that this method did a good job of identifying the start of the dendritic spike to within about one sample (~0.1 ms). Because of the low amount of recording noise, the start of the AP was computed as where the slope of the rising phase of the AP intersected a 40 mV/ms threshold (measured to within 0.01 ms with linear interpolation).

Because of the variability in our estimate of the start of the dendritic spike, we applied a conservative latency criterion of at least 0.2 ms to classify a somatic AP as following the dendritic spike. This resulted in 64 APs with latencies < 0.2 ms. Most recordings had mean AP latencies > 1 ms, which was much greater than our potential latency measurement error.

Temporal selectivity of soma APs. In five experiments, we recorded from both the dendrite and soma while the signal-only and signal+noise stimuli were injected. To measure the selectivity of soma APs, we estimated the probability of observing a soma AP following a particular signal. Because we set the amplitude of the injected waveforms to threshold, the probability of observing a soma AP was low, even for the preferred 10–90% rise times. We then plotted the peak soma AP probability vs. signal rise time and fit with a Gaussian (*Eq. 13*).

RESULTS

We made whole cell recordings from the distal apical trunk and primary tuft branches of mouse PT L5 pyramidal dendrites (Dembrow et al. 2010, 2015; Kalmbach et al. 2013, 2015) (median location 280, range 50–380 μm, $N = 29$). L5 PT neurons in mouse PFC are located ~450–600 μm from the pial surface, with the apical tuft starting at the L1-L2/3 border (Fig. 1*A*). Our recording locations spanned the entire extent of the main apical trunk and the proximal part of the apical tuft. However, all recordings from the apical trunk, with the exception of two, were within 70 μm of the nexus of the apical tuft, near the L1-L2/3 border, and three recordings were slightly distal to the nexus (red dots, Fig. 1*A*). Thus, our results mainly address dendritic integration near the nexus of the apical tuft in L5 pyramidal neurons of PFC.

We applied a systems approach to study how the dendrites integrated arbitrary current injections. The dendritic stimuli were long periods (1–2 min) of noise, waveforms, or a combination of the two (examples shown in Fig. 1*B*). Functional models (summarized in Fig. 1*C*) were used to describe the dendritic membrane potential (V_{dend}), dendritic nonlinearity (I_{NL}), and somatic potential (V_{soma}) in response to our dendritic stimuli. Our results below systematically develop the structure and rationale for each model as we characterize the dendritic nonlinearities.

Although dendritic current injections do not reproduce the conductance changes associated with in vivo synaptic input, a noise input has several advantages for characterizing dendritic signal processing: *1*) Bypassing the synaptic contributions

allowed the dendritic component to be isolated and described with functional components. *2*) The noise stimulus contained a wide constellation of frequency components that dendrites may experience in vivo, thus mimicking the fast fluctuations caused by the background activity of the thousands of synapses on cortical dendrites. *3*) It facilitated the application of systems-identification techniques to construct and test functional models (Hunter and Korenberg 1986; Sakai 1992; Wu et al. 2006).

Linear component of dendritic response. In the first 15 experiments, the variance of the injected current was set to produce either sub- or suprathreshold responses on alternating stimulus presentations (referred to as small and large noise; Fig. 2*A*). Figure 2*B* shows examples of the injected current stimulus (black) and dendritic membrane potential (V_{dend}, blue) for a recording 275 μm from the soma. Across the population, the small-noise condition produced depolarizations from rest of only a few millivolts (mean 1.7 ± 0.1, max 11.5 ± 2.3 mV), while the large noise resulted in substantial dendritic depolarizations (mean 7.8 ± 0.4, max 80.3 ± 2.1 mV) and somatic APs (addressed below).

We first isolated the linear component of the dendritic signal processing by fitting a linear filter (*D*) to each input condition (Fig. 2*C*). The linear filter was optimized (see MATERIALS AND METHODS) such that when it was convolved with the noise current injection it produced a linear prediction of the dendritic potential (V_L; orange, Fig. 2*C*). Example dendritic filters for three cells are shown in both the time and frequency domains in Fig. 2*D*. The filters had relatively broad frequency responses with a peak at ~8 Hz, and their impulse response function had 10–90% decay times that differed by <1 ms between small and large noise ($P < 0.001$, paired *t*-test, $N = 15$). As

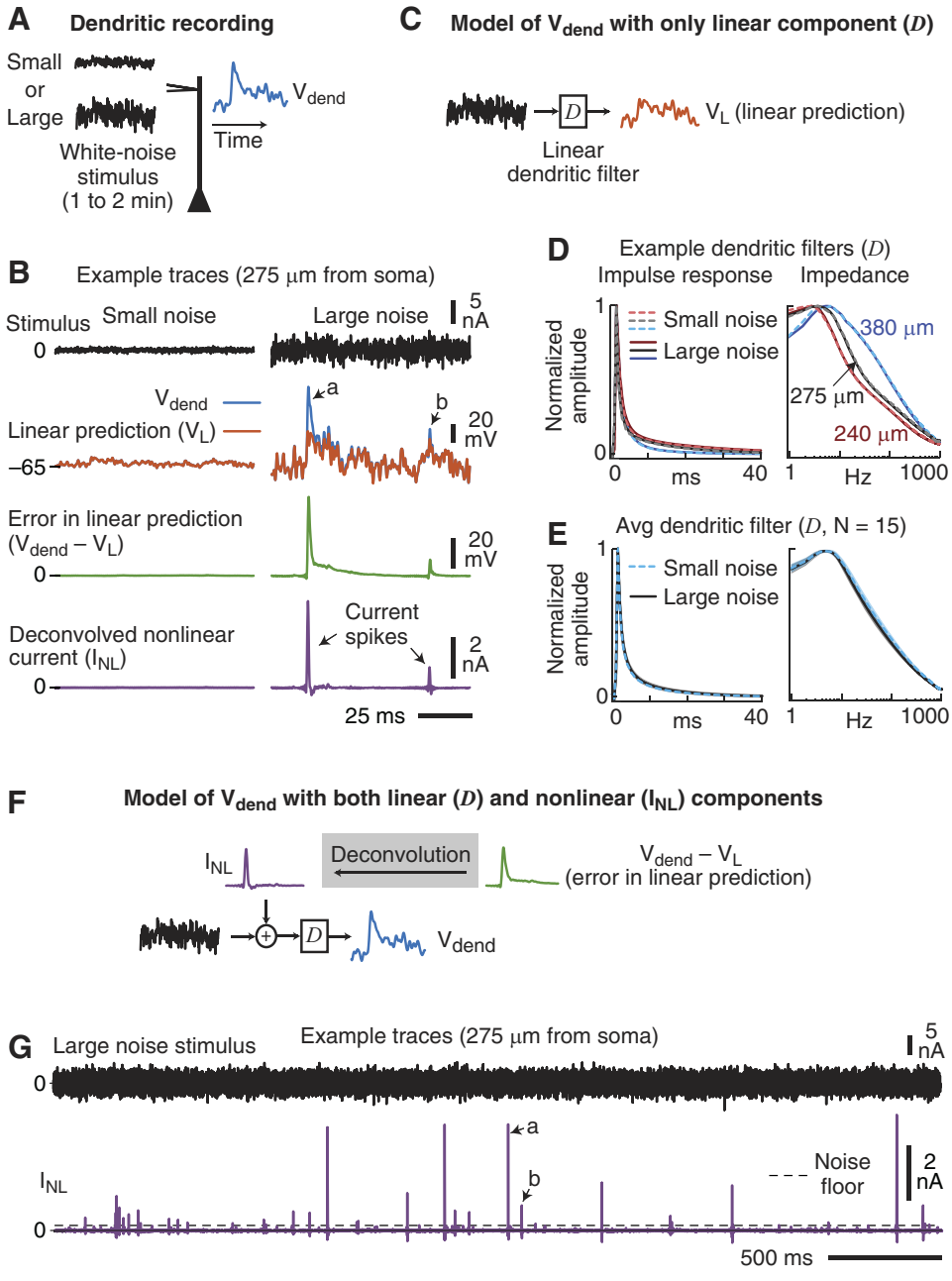

Fig. 2. Isolating the linear and nonlinear components of the dendritic membrane potential. *A*: the membrane potential in the dendrite was recorded (V_{dend}) in response to small- and large-amplitude Gaussian-distributed white-noise current injections. *B*: example traces from a dendritic recording 275 μm from the soma for the small (*left*)- and large (*right*)-amplitude white-noise stimuli. Traces show the recorded membrane potential (blue), linear prediction (V_L, orange), and nonlinear component (I_{NL}, purple) of the dendritic membrane response. For the small-noise stimulus, the linear prediction overlapped the measured dendritic potential. *Arrows a* and *b* denote large and small errors (green), respectively, in the linear prediction (V_L) during the large-noise stimulus. *C*: the linear component of the dendritic response was modeled as a linear filter (*D*). Convolving the linear dendritic filter with the white-noise stimulus produced the linear prediction (V_L, orange) of the dendritic potential. *D*: example linear dendritic filters (*D*) from 3 dendritic recording locations for the small (dashed)- and large (solid)-noise stimuli. *Left*: normalized impulse response functions. *Right*: normalized impedance amplitude profiles. The distance of the dendritic recording electrode from the soma is labeled. *E*: average linear dendritic filters for the small- and large-noise stimuli. Shading is SE. *F*: the nonlinear component of the dendrites was modeled as a current (I_{NL}, purple) added to the stimulus. I_{NL} was estimated from the voltage errors in the linear prediction (green) by deconvolution. By mathematical definition, when the injected stimulus + I_{NL} was convolved with the dendritic filter, this model reproduced the measured dendritic potential (blue). Thus, I_{NL} represented the contribution the dendrites made to the dendritic stimulus current. *G*: extended example trace of the nonlinear component (I_{NL}) in response to the large-noise stimulus. I_{NL} was composed of mostly inward depolarizing current spikes of varying amplitudes. *Arrows a* and *b* correspond to the same nonlinear dendritic current spikes in *B*. Dashed line (noise floor) is the minimal I_{NL} amplitude used for the identification of individual dendritic spikes (see MATERIALS AND METHODS).

illustrated in Fig. 2*D*, filters systematically decayed faster as dendritic location increased ($R = -0.82$, $P < 0.001$).

The average dendritic filters (Fig. 2*E*) show that across the population filters were very similar between the small- and large-noise stimuli. Thus, the linear component of the dendritic membrane potential (*D*) was relatively invariant to stimulus amplitude.

We next compared the linear prediction of the dendritic membrane potential (V_L), obtained by convolving the dendritic filter with the noise stimulus, to the actual recorded dendritic potential (V_{dend}). As illustrated in Fig. 2*B*, for the small-noise condition V_L (orange) completely overlapped the measured V_{dend} (blue) and thus perfectly reproduced the dendritic potential. Across the population, the variance accounted for (VAF) by the dendritic filter in the small-noise condition was on average 99.8 ± 0.1% ($N = 15$). Thus, the dendritic potential was fully described by the linear filter (*D*) during small random inputs.

The linear filter was comparatively less able to predict the dendritic potential during the large-amplitude noise (VAF = 96.2 ± 0.7%). Inspection of the linear prediction (V_L vs. V_{dend}; Fig. 2*B*) revealed that the dendritic response also contained a nonlinear component that produced additional depolarizations during the large noise (*arrows a* and *b*). Although the linear component (*D*) did not change as the stimulus became larger, it accounted for less of the dendritic membrane potential.

Isolating nonlinear component of dendritic response. Inspection of the errors in the linear fit (green, Fig. 2*B*) revealed stable periods of linearity (i.e., error near 0) interspersed with voltage errors of different amplitudes. Importantly, the errors were typically positive and exhibited a fast rise time followed by a slow decay that approximated the shape of the dendritic filter. This suggested that the voltage errors could be modeled as current impulses located at the input to the dendritic filter (Fig. 2*F*).

We used deconvolution to transform the voltage error (green) into a nonlinear current (I_{NL}, purple) that was added to the dendritic stimulus (Fig. 2*F*). In all figures, a positive I_{NL} represents depolarizing current injected into the dendrite. By definition, convolving the dendritic filter with I_{NL} + the noise stimulus reproduced 100% of the dendritic membrane potential.

Relationship of model to passive and active properties of dendrites. Transforming the nonlinear component of the dendritic response from a voltage error into a current (I_{NL}) was a novel step in our analysis. I_{NL} represents a model of the net current produced by ion channels that are known to contribute to the generation of dendritic nonlinearities (including Na^+ and Ca^{2+} channels). Importantly, I_{NL} provides a precise description of the dendritic nonlinearity in response to arbitrary stimulus patterns, which cannot be gleaned from a casual observation of the dendritic membrane potential alone.

Our model in Fig. 2*F* is closely related to the passive and active properties that have been traditionally been used to quantify the dendritic response. The linear component of the model (*D*) captures the linear passive membrane response plus any contributions by voltage-gated channels that behave in a linear fashion. Thus, the nonlinear component, I_{NL}, represents the contribution of active properties that cannot be captured by a linear model. Separating the contribution of voltage-gated channels into their linear and nonlinear components allows us to focus only on the nonlinear active properties.

Properties of nonlinear component (I_{NL}). As shown by the example trace on a longer timescale (Fig. 2*G*), I_{NL} consisted of mainly brief, inward, current spikes of varied amplitude. We next quantified the properties of these dendritic current spikes. First, we wanted to know whether the amplitude of a dendritic spike depended on the amplitude of previous dendritic spikes. Across all 29 experiments that used the large-noise stimulus, the average autocorrelation function of I_{NL} was relatively flat, exhibiting only a weak positive correlation within ~25 ms (Fig. 3*A*). Thus, dendritic spike timing and amplitude were largely independent, with a slight tendency of spikes to cluster within 25-ms bursts.

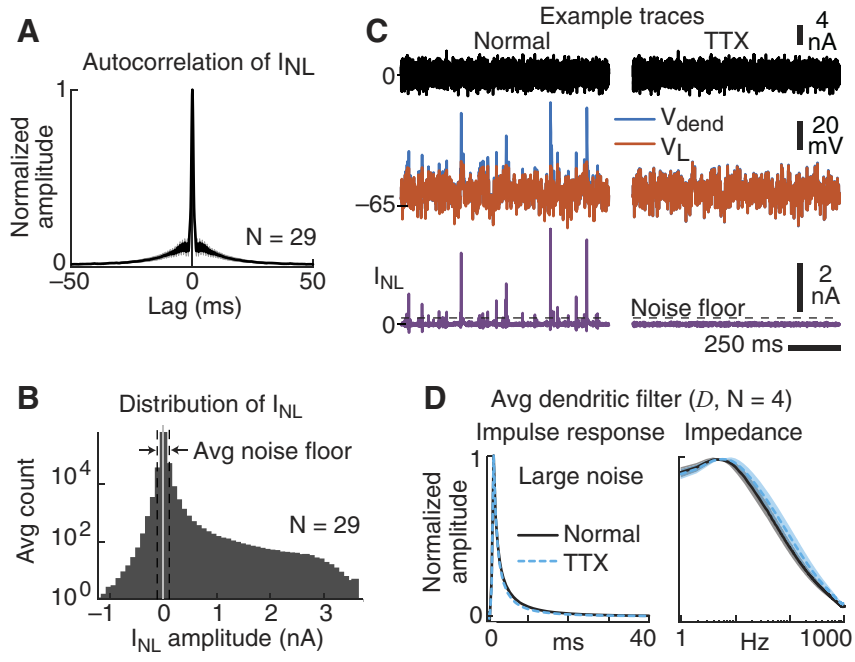

Fig. 3. Properties of the nonlinear current (I_{NL}). *A*: the average autocorrelation function of the nonlinear current (I_{NL}) shows a weak correlation within a ~25-ms window. *B*: amplitude histogram of I_{NL} averaged across all recordings. All neurons contributed to each bin. The average noise floor refers to the three-sigma distribution around zero (see MATERIALS AND METHODS). *C*: example traces to the same noise pattern before and after application of TTX. Errors in the linear component (V_{dend} vs. V_L) and nonlinear current spikes in I_{NL} were completely eliminated by application of TTX. Similar effects were observed in all 4 TTX experiments. Two experiments bath applied TTX, and two had local application of TTX to the dendrites (see Fig. 7, *F–I*). *D*: the average linear dendritic filter (*D*) was relatively unaffected by the application of TTX. *Left*: normalized impulse response functions. *Right*: normalized impedance amplitude profiles. Shading is SE.

Because deconvolution can enhance experimental noise, we next examined the reliability of I_{NL}. The timing and amplitude of dendritic spikes were nearly identical between presentations of the same stimulus (data not shown; see MATERIALS AND METHODS), suggesting that I_{NL} was directly linked to the stimulus pattern injected into the dendrites, with minimal effects of experimental noise.

To isolate individual dendritic spikes we needed to first quantify the noise levels in I_{NL}. The average amplitude distribution of I_{NL} was positively skewed, reflecting a range of inward current spike amplitudes that produced membrane depolarization (Fig. 3*B*). Large negative portions of I_{NL} presumably reflected active conductances involved in membrane repolarization. Small amplitude variations around zero likely represented the experimental noise in I_{NL}. The three-sigma noise level (equivalent to 99.7% of the noise) was estimated separately for each cell (referred to as the noise floor, vertical dashed lines in Fig. 3*B*; see MATERIALS AND METHODS). Individual I_{NL} spikes with amplitudes above the noise floor were classified as dendritic current spikes. As illustrated by the example I_{NL} trace in Fig. 2*G*, isolated dendritic spike amplitudes above the noise floor varied by over a factor of 10 in single neurons.

Across the population ($N = 29$), isolated dendritic current spikes occurred at a mean rate = 25 ± 12 (SD) spikes/s and had an average width at half-height = 0.7 ± 0.05 (SD) ms. Small dendritic spikes tended to have a symmetrical shape, possibly due to the 2 kHz sampling rate used in our analysis (see MATERIALS AND METHODS). As we show below, however, many large dendritic spikes, especially those preceding somatic APs, had nonsymmetrical features. In addition, application of 1 μM TTX completely eliminated all I_{NL} spikes ($N = 4$, example traces shown in Fig. 3*C*) but had no appreciable effect on the linear component of the dendrite (filter *D*; Fig. 3*D*).

In summary, the properties of I_{NL} suggest that during the random noise input the nonlinear component of the dendritic signal processing was composed of mainly Na^+ channel-mediated current spikes that were tightly linked to the stimulus, occurred at a relatively fast rate, and were highly variable in amplitude.

Dendritic current spike amplitude was correlated with stimulus rise time. What do the amplitude and timing of a dendritic current spike tell the neuron about the injected stimulus? In other words, why did the dendrite sometimes produce small-amplitude spikes while at other times it produced large spikes? As illustrated by the two example dendritic current spikes in Fig. 4*A* (1 large at 5.2 × noise floor and 1 small at 1.1 × noise floor), the largest stimulus fluctuations (arrows) did not coincide with the occurrence of a spike, while a steady rise of the stimulus seemed to precede each spike, especially the larger spike.

To quantify what a dendritic current spike tells the neuron about the stimulus, we applied the STA theorem. This theorem states that in response to white noise the stimulus STA is the input feature that best predicts when a spike occurs (Bryant and Segundo 1976; de Boer and Kuyper 1968). Thus, we binned well-isolated dendritic current spikes by amplitude and averaged the noise stimulus centered on each spike (Fig. 4*B*; see MATERIALS AND METHODS).

Across the population, 23,820 isolated dendritic I_{NL} spikes were grouped into eight amplitude bins, with every cell contributing to each bin. The stimulus STA (Fig. 4*B*, black) revealed that dendritic spikes, regardless of amplitude, were on average preceded by similar fast-rising current injection waveforms. It should be noted that while the large-noise stimulus contained amplitudes exceeding 5 nA, the STA amplitude preceding a dendrite spike was far less (~1.5 nA). This is also seen in the example trace in Fig. 4*A*, where large instantaneous current injections (arrows) did

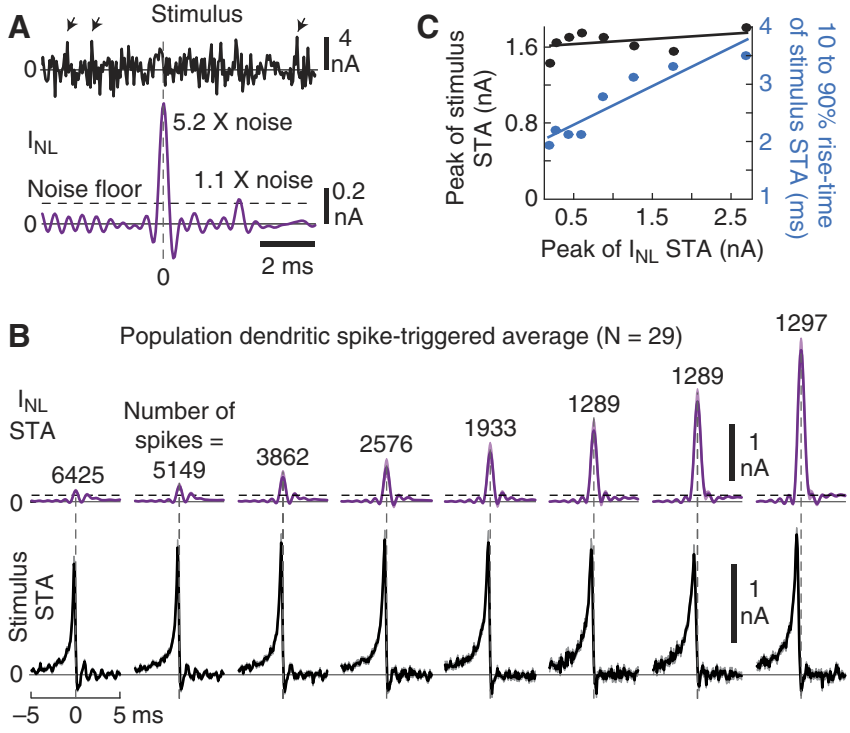

Fig. 4. Spike-triggered averages (STAs) reveal the link between dendritic current spikes and the input stimulus. *A*: example trace of I_{NL} (purple) showing 2 dendritic current spikes (one 5.2 × and the other 1.1 × noise floor). The stimulus (black) highlights that fast, large, stimulus fluctuations (arrows) were not followed by a dendritic spike. *B*: STAs of the dendritic current spikes (purple) and stimulus (black), grouped by dendritic current spike amplitude and aligned to the peak of the spike (0 ms). STAs were computed based on 23,820 dendritic current spikes isolated from I_{NL} (see MATERIALS AND METHODS) and show the average across all 29 experiments. Note that the peak of the current spike STA increased, while the peak of the stimulus STA was relatively flat. Because of the nonuniform distribution profile of I_{NL} (see Fig. 3*B*), more spikes contributed to the smaller-amplitude STA bins. Dashed line is the noise floor, and shading is SE. *C*: the 10–90% rise time (blue), but not the peak amplitude (black), of the stimulus STA increased as a function of dendritic current spike size.

not produce dendritic spikes. Thus, the STA results reveal that nonlinear dendritic spikes tend to follow a particular shape (or feature) in the dendritic input.

What stimulus feature determined the amplitude of the dendritic spike? Although the peak amplitude of the average current spike increased by over a factor of 10 (Fig. 4*B*, purple), the peak of the stimulus STA was surprisingly flat over the wide range of spike amplitudes ($R = 0.41$, $P = 0.31$; Fig. 4*C*, black). In comparison, the 10–90% rise time of the stimulus STA steadily increased as a function of spike amplitude ($R = 0.93$, $P = 0.001$; Fig. 4*C*, blue). Thus, small differences in the rise time of the stimulus STA, but not necessarily the amplitude, were correlated with dendritic current spike amplitude.

The STA results are important because they suggest that the amplitude of the dendritic spike informs the neuron about the shape of the injected dendritic input. A 10–90% stimulus rise time of ~4 ms tended to produce the largest dendritic spikes, while faster rise times produced smaller dendritic spikes. Thus, the nonlinear component of the dendritic signal processing is selective to a particular input feature.

Simple cascade model predicted dendritic spike timing and amplitude. Although the stimulus STAs in Fig. 4*B* represent the shape of the stimulus waveform that best predicts the amplitude of a dendritic current spike, it does not reveal how good such a model would be. Thus, we constructed a common two-stage cascade model (Hunter and Korenberg 1986) of the dendritic nonlinear component to reproduce I_{NL} as a function of the stimulus input (Fig. 5*A*; see MATERIALS AND METHODS).

The first stage of the model convolved the stimulus with a linear "spike" filter (*S*). The output of the spike filter (*x*) was

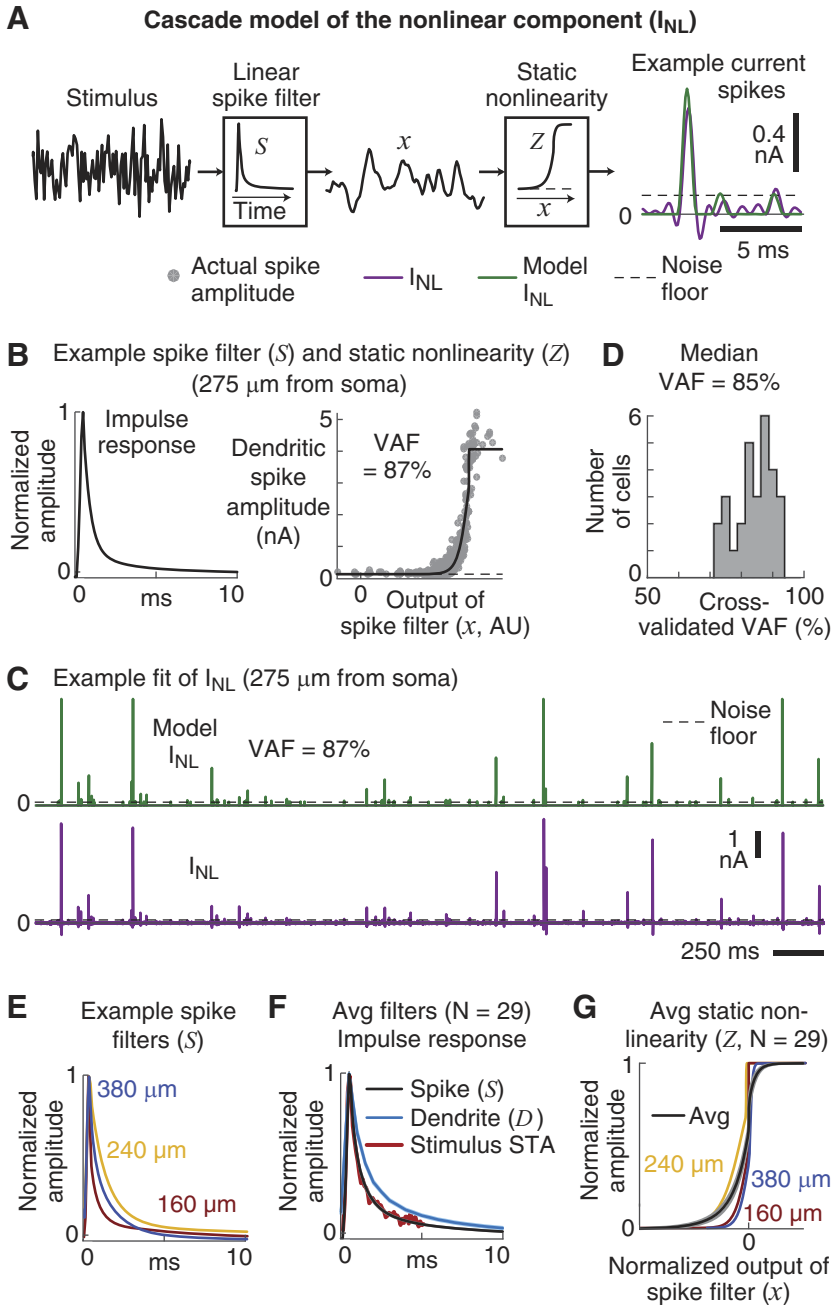

Fig. 5. Dendritic current spikes are described by a linear-nonlinear cascade model. *A*: the nonlinear dendritic current (I_{NL}, purple) was modeled as a linear filter (*S*, referred to as a spike filter) that was convolved with the stimulus, followed by a sigmoidal-shaped static nonlinearity (*Z*). See MATERIALS AND METHODS for details. Shown is an example model current spike (green) that overlaps the actual current spike (purple). *B*: example impulse response function of the spike filter and static nonlinearity for a single neuron. For each neuron, the model was fit to isolated spikes with amplitudes ≥ the noise floor (gray points). The error in the fit is the difference between the actual spike amplitude and the static nonlinearity. For this neuron, the 2-fold cross-validated variance accounted for (VAF) by the model was 87%. *C*: extended example traces of the nonlinear dendritic current (I_{NL}) highlight the ability of the model (green) to reproduce the observed dendritic current spike times and amplitudes (purple). *D*: distribution of the 2-fold cross-validated VAF by the model of I_{NL} for all cells. *E*: example impulse response functions for spike filters from 3 dendritic locations. *F*: average impulse response function for the spike filter (*S*, black) and dendritic filter (*D*, blue) across all 29 recordings. Note that the average spike filter is the same as the average time-reversed STA of the stimulus for the largest dendritic spikes (red, replotted from Fig. 4*B*). *G*: average static nonlinearity (*Z*, black). To show the average shape of the static nonlinearity, for each neuron *Z* was normalized to its maximum amplitude and shifted so that its midpoint ($x0$ in *Eq. 11*) was aligned at 0 on the *x*-axis. Three example static nonlinearities are shown in color and correspond to the same dendritic locations shown in *E*. Shading is SE (no visible shading indicates SEs smaller than line widths).

then passed through a static nonlinearity (*Z*) that produced current spikes of variable amplitude. We optimized the model separately for each cell, using isolated dendritic spikes that were greater than or equal to the noise floor. Figure 5*A* shows a short example trace of the optimized model I_{NL} output (green) vs. the actual I_{NL} (purple).

A neuron's optimized spike filter and static nonlinearity are shown in Fig. 5*B*, and the model I_{NL} output is shown in Fig. 5*C* on a longer timescale. For this dendritic recording, the model reproduced the spike amplitudes reasonably well (cross-validated VAF = 87%), which can be observed by how close the true dendritic spike amplitudes (gray points, Fig. 5*B*) are to the fitted static nonlinearity (*Z*, black sigmoid-shaped curve). Across all 29 recordings, the cascade model accounted for dendritic current spike time and amplitude with a median cross-validated VAF = 85% (Fig. 5*D*).

As illustrated by the example model fit in Fig. 5*C*, ~98% of the time I_{NL} was below the noise floor, and these data were not used to optimize the model. Thus, we used these nonspiking periods to further validate the model and found that "false-alarm" model current spikes (i.e., model spikes with no corresponding real dendritic spikes) were highly unlikely. For example, across all cells, the average rate of model false-alarm spikes with amplitudes at least 3 × noise floor was a negligible 0.01 ± 0.003 spikes/s. The high VAF and the low false-alarm spike rate of the model suggest that a functional cascade was reasonably good at capturing the nonlinear component of the dendritic signal processing.

The spike filter shape was fairly similar for different dendrite locations (impulse response functions for 3 example filters are shown in Fig. 5*E*). Across the population, the decay time of the spike filter's impulse response function was not strongly linked to dendritic location ($R = -0.36$, $P = 0.06$, $N = 29$). The average spike filter (*S*; Fig. 5*F*, black) was slightly faster than the average dendritic filter (*D*; blue), with a 10–90% decay = 4.2 ± 0.3 ms (*S*) vs. 6.9 ± 0.4 ms (*D*) ($P < 0.001$, paired *t*-test). As predicted by the STA theorem, the shape of the average spike filter was identical to the stimulus STA of the largest spikes shown in Fig. 4*B* (replotted in Fig. 5*F*, red). The average static nonlinearity (*Z*; black, Fig. 5*G*) had a relatively consistent shape across cells in the form of a sigmoid that increased in slope as it approached the maximum spike amplitude. From visual inspection, the static nonlinearity did not appear to be dependent on dendritic location (3 examples are shown in color in Fig. 5*G*).

Dendritic current spikes were selective to rise time of stimulus. The results so far suggest a model of the dendritic membrane potential that is based on linear and nonlinear components (Fig. 6*A*). This model makes specific predictions that can be experimentally tested. For example, the cascade model of the nonlinear component (I_{NL}) predicts that dendritic current spike amplitudes will be selective to the shape of the input waveforms (Fig. 6*B*). Dendritic inputs that match the time-reversed shape of the spike filter (*S*), even in the presence of noise, will produce the largest-amplitude current spikes (Fig. 6*B*, *left*). Smaller dendritic spikes will correspond to inputs that are less similar to *S* (i.e., a nonmatched stimulus; Fig. 6*B*, *right*). Thus, we tested this hypothesis by experimentally measuring the selectivity of the dendritic nonlinearity using waveform stimuli that were very different from the white noise used to develop the cascade model of I_{NL}. We then compared the actual selectivity of the dendrite's nonlinearity to that predicted by the model.

We alternated between three 1-min-long stimulus conditions (Fig. 6*C*). In the first condition we injected the same large-amplitude white noise as above. The second, "signal-only," condition consisted of a randomized series of nine different equal-energy signals that were either time compressed or stretched versions of the average time-reversed spike filter (*S*) derived from the cascade model fits. A short example trace of the "signal-only" input is shown in Fig. 6*D*. For the third, "signal+noise," condition, we presented the same equal-energy signals embedded in half-amplitude white noise. A prediction of the cascade model of I_{NL} is that additive noise should broaden the selectivity but not change the dendrite's preferred input waveform. It should be noted that the waveforms were normalized to have equal energy so that only the rise time, and not the signal strength, varied between each of the nine waveforms (see MATERIALS AND METHODS).

As highlighted by the example traces in Fig. 6*E*, *center*, a large dendritic current spike (purple, *arrow a*) occurred in response to a matched signal waveform with a rise time of 2.5 ms but not to a faster, nonmatched, input of 0.8 ms (*arrow b*). The same preferred signal also produced a large dendritic spike in the signal+noise condition (Fig. 6*E*, *right*). Note that dendritic spike amplitudes for the two signal conditions (Fig. 6*E*, *center* and *right*) tended to be smaller than spikes produced during the large noise (Fig. 6*E*, *left*). This was likely due to moderate Na^+-channel inactivation, as the two "signal conditions" were no longer zero-mean stimuli.

To measure the selectivity of the dendritic nonlinearity, we plotted the average peak amplitude of the dendritic current spikes (I_{NL}) vs. the 10–90% rise time of the input stimulus (an example cell is shown in Fig. 6*F*, *top*). Across our 14 cells, the amplitude of the dendritic spike that followed each signal presentation was selective to the stimulus rise time. On average, the largest dendritic spikes occurred in response to signals with rise times between 4 and 5 ms (Fig. 6*G*, *top*).

The selectivity of the I_{NL} was approximately Gaussian as a function of the log rise time (solid lines in Fig. 6, *F* and *G*, are Gaussian fits). We used the mean (μ) and standard deviation (σ) of the fitted Gaussians to characterize the selectivity. There was a substantial broadening of the selectivity (σ) for the signal+noise (orange) vs. signal-only (blue) conditions (mean = 6.1 vs. 2.2, $P < 0.0001$, paired *t*-test, $N = 14$). In comparison, the preferred rise time (μ) was the same between the two conditions (mean = 4.5 and 4.4 ms, $P = 0.64$). Thus, the addition of noise broadened the selectivity of the dendritic nonlinearity, with no change in the preferred stimulus feature. Neither μ or σ was correlated with dendritic recording location (Pearson's, $P > 0.24$ for both parameters and conditions).

The cascade model of I_{NL} reproduced the dendritic spikes observed in the two signal conditions (an example model trace is shown in Fig. 6*E*, green). The I_{NL} model used the same spike filter (*S*) estimated from the large-noise condition, but we refit the static nonlinearity (*Z*) to accommodate the reduced spike amplitude for the two signal conditions (see MATERIALS AND METHODS). Comparison of the cascade model and cell selectivity curves (Fig. 6, *F* and *G*, *bottom*) revealed that the model captured much of the stimulus selectivity of the dendritic spikes and predicted the much wider selectivity in the presence of noise (orange vs. blue). A cell-by-cell comparison of the center (μ) and

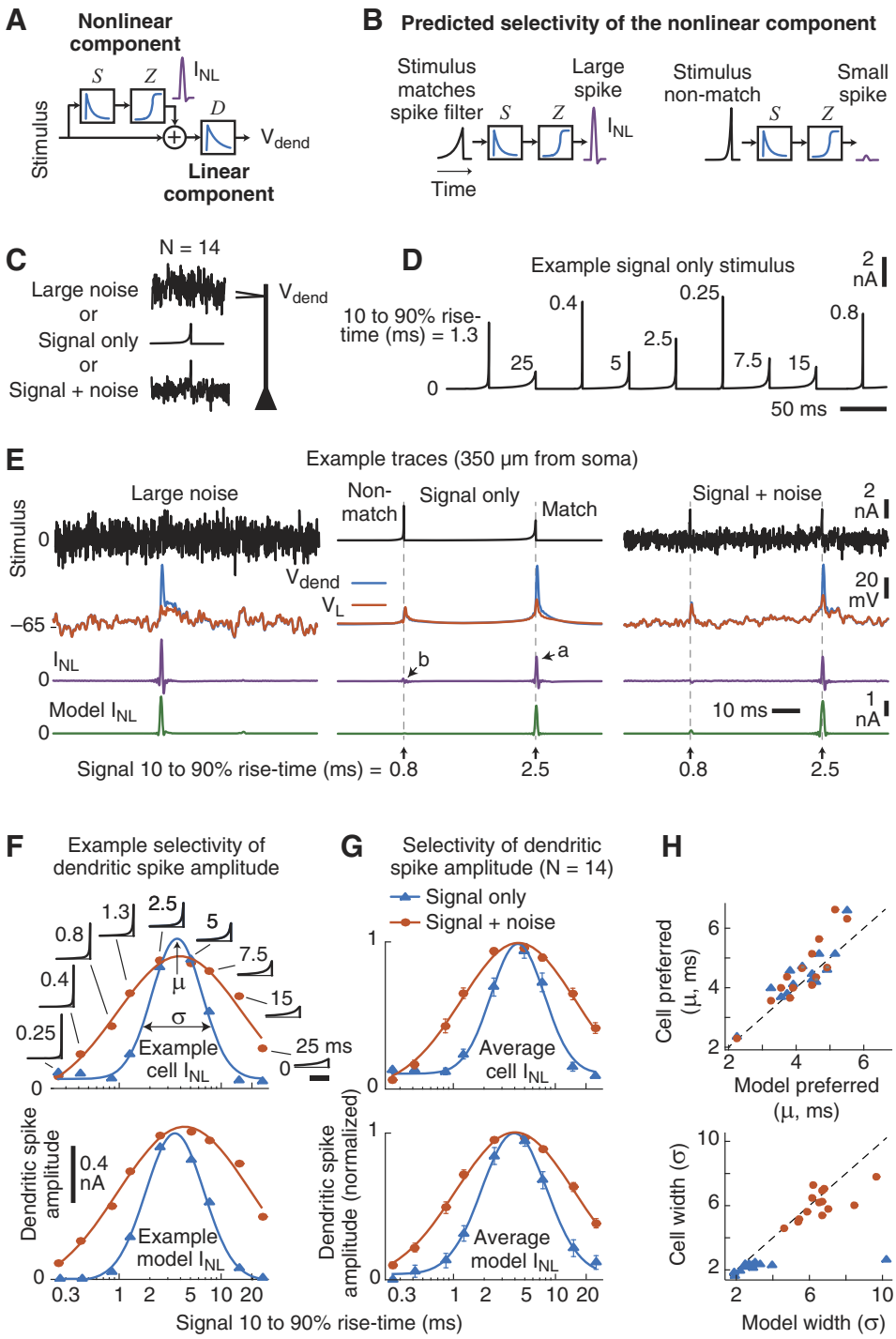

Fig. 6. Dendritic current spike amplitude is selective for temporal features of the input. *A*: summary of the model for the linear and nonlinear components of the dendritic membrane potential. *B*: this model predicts that for equal-energy input signals arriving at the dendrite the linear spike filter (*S*) will produce a maximum response to a signal that is matched to its time-reversed shape (i.e., the impulse response function). This is usually referred to as the matched-filter theorem. *C*: 14 new experiments were performed using 3 dendritic current injections: *1*) large white noise; *2*) signal only—a random series of 9 different signals, presented every 50 ms, that were the time compressed (or stretched) versions of the time-reversed impulse response function of the spike filter (*S*; Fig. 5*E*); *3*) signal+noise—the same "signal-only" pattern + half-amplitude white noise. *D*: example trace of the signal-only stimulus. The 10–90% rise time (ms) is shown next to each signal waveform. *E*: example responses of a neuron and model are shown for each stimulus condition. Note that dendritic current spikes (purple) are largest for the matched stimulus, even in the presence of noise. See text for references to arrows. *F* and *G*: example (*F*; same cell as *E*) and average (*G*) selectivity for the neuron (*top*) and model (*bottom*) dendritic current spikes. The peak of the average I_{NL} that occurred after each signal waveform was plotted as a function of the signal's 10–90% rise time for the signal-only (blue) and signal+noise (orange) conditions. Note that the *x*-axis is a log scale and the solid lines are Gaussian fits. *Insets* in *F* show the signal waveforms injected into the dendrites (scale bar, 5 ms). Error bars are SE. *H*: the cell-by-cell preferred rise time (μ) and width (σ), as determined by the Gaussian fits, were well accounted for by the model, with the exception of a single outlier in the signal-only condition. As predicted by the cascade model of I_{NL}, the addition of noise increased the width of the selectivity but did not change the dendritic nonlinearity's preferred rise time.

width (σ) of the selectivity curves further highlights the model's good performance but also reveals a slight shift in both parameters (Fig. 6*H*). Model I_{NL} selectivity tended to be a little wider and centered on slightly faster rise times.

In summary, the nonlinear mechanism that generates dendritic Na^+ spikes (I_{NL}) in mouse PT L5 neurons is selective to the input dynamics as predicted by the functional model (Fig. 6, *A* and *B*). Although the linear spike filter (*S*) captured the selectivity of the dendritic nonlinearity, changes in the static nonlinearity (*Z*) across conditions revealed an input-dependent reduction of the dendritic spike amplitude. Importantly, the injected waveforms further validated the cascade model of I_{NL} using stimuli that were dramatically different from the white noise originally used to derive the model's spike filter (*S*). This is especially evident from the fact that the model accurately predicted how the addition of noise (signal+noise condition) would widen the selectivity without affecting the preferred input dynamics.

Most somatic APs followed dendritic current spikes. Thus far we have focused only on the dendritic nonlinearity (I_{NL}) and found that it was selective to a particular input shape as predicted by the functional model of I_{NL}. How does the dendritic nonlinear component contribute to the neuron's abil-

ity to produce a somatic AP? Although it has been shown that dendritic Na^+ spikes exert a strong influence on somatic APs (Gasparini and Magee 2006; Golding and Spruston 1998; Sivyer and Williams 2013; Smith et al. 2013; Stuart et al. 1997), our novel approach for isolating dendritic spikes using a noise stimulus and deconvolution warranted that we also examine this question in detail. In 16 experiments, we simultaneously recorded the somatic and dendritic membrane potential, using the large white-noise stimulus (Fig. 7*A*). In these recordings, the dendritic electrode location ranged from 50 to 380 μm from the soma (median 268 μm), with the majority of recordings centered on the nexus of the apical tuft (see Fig. 1*A*).

For each simultaneous somatic and dendritic recording, we extracted the dendritic nonlinear current (I_{NL}) from the dendritic membrane potential as described above. Across all cells, in response to the white-noise stimulus somatic APs occurred at a mean rate of 1.0 ± 0.9 (SD) spikes/s, much less than the ~25 spikes/s of the dendritic spikes. Note that the term "somatic AP" referrers to the somatic recording location and not the site of AP initiation, which has been shown to be in the axon (reviewed in Bean 2007; Kress and Mennerick 2009).

The higher rate of dendritic spikes vs. somatic APs agrees with previous in vitro observations that not all dendritic spikes are followed by APs (Gasparini and Magee 2006; Golding and Spruston 1998; Stuart et al. 1997) and that small dendritic spikes can occur at higher firing rates compared with somatic APs during in vivo or intact-circuit recordings (Sivyer and Williams 2013; Smith et al. 2013). However, our ratio of dendritic spike to AP firing rate was greater than that previously observed. Two potential reasons for this are that *1*) the high variance in our noise stimulus produced more dendritic spikes and *2*) the deconvolution method was able to resolve smaller dendritic spikes (just above the noise floor).

As illustrated in the example traces in Fig. 7*B*, dendritic current spikes (I_{NL}, purple) almost always preceded somatic APs (blue). Note that sometimes a small bump in the falling phase of the dendritic spike was observed, presumably due to AP back-propagation (Fig. 7*B*, *left*, *arrow a*). Somatic APs occasionally followed bursts of two or more smaller dendritic current spikes, where the first spike had a subthreshold depolarizing effect on the soma (Fig. 7*B*, *center*, *arrow b*). When the latency between the dendritic current spike and somatic AP was long, we typically observed isolated back-propagating spikes in the form of a second smaller I_{NL} spike immediately following the AP (Fig. 7*B*, *right*, *arrow c*). Of the 3,241 individual somatic APs recorded in our 16 experiments, ~98% followed a large dendritic current spike (see MATERIALS AND METHODS). Many large dendritic current spikes, however, were not followed by somatic APs (Fig. 7*C*), and we focus our analyses on these spikes below.

Although our AP firing rates were lower than typically observed in vivo, ~15% of somatic APs were part of a burst containing two or more APs within a 25-ms window (data not shown). During these AP bursts, I_{NL} typically contained dendritic spikes riding on top of a small, sustained, inward current. This weak bursting in our data was revealed above by the small positive autocorrelation in I_{NL} (see Fig. 3*A*).

About 2% of the somatic APs (64 of 3,241 total APs recorded) were not preceded by a large dendritic spike (observed in 9 of 16 experiments). As shown by the example traces in Fig. 7*D*, large dendritic current spikes occasionally occurred just after the somatic AP. Presumably a large dendritic spike just after the AP reflected the back-propagation of the somatic AP into the dendrites.

Considering only dendritic spikes that immediately preceded somatic APs, we found that the average latency of the somatic AP increased as a function of dendritic location (Fig. 7*E*), which agrees with previous observations with nonnoise current injections (Stuart et al. 1997). To further confirm that somatic APs were causally linked to the dendritic nonlinearities, in two experiments we applied TTX locally at the dendrite while recording the somatic and dendritic responses (Fig. 7*F*). Locally blocking Na^+ channels at the dendrite eliminated all dendritic spikes and somatic APs in response to the dendritic noise input (Fig. 7*G*). The example traces show that TTX reduced I_{NL} below the noise floor threshold for a dendritic spike (Fig. 7*H*). For both experiments, however, a brief somatic current injection still produced a somatic AP in the presence of the local TTX on the dendrites but attenuated the back-propagation of the AP into the dendrites (Fig. 7*I*). Note that the somatic AP threshold in response to somatic current injection was unchanged by the TTX puff in the dendrite (*cell 1* threshold went from −52.6 mV to –51.3 mV and *cell 2* threshold went from –52.7 mV to –52.5 mV, baseline vs. TTX, respectively).

Functional model revealed that soma linearly integrated boosted dendritic spikes. In response to the noise stimulus, a vast majority of the nonlinear dendritic current spikes (~25 spikes/s) were not associated with somatic APs (~1 spike/s). What was the relationship between the dendritic spike and the soma membrane potential when there was no somatic AP? For example, were dendritic spikes integrated at the soma in the same way as the stimulus? Or was the soma potential affected by additional nonlinearities not captured by the dendritic I_{NL}?

To answer these questions, we constructed two functional models of the subthreshold somatic potential (Fig. 8*A*): *1*) a linear model that only used the stimulus as the input and *2*) a linear model that also included the nonlinear dendritic current I_{NL}. The first model convolved the stimulus with a linear soma filter (*G*) to reproduce the somatic potential (yellow). The second model convolved the stimulus + a boosted version of I_{NL} (green) with *G* to produce V_{soma} (orange).

Because I_{NL} is a measure of the local nonlinearity in the dendrite, the boost function (*B*) allowed the effect of I_{NL} on the soma to vary. For example, nonlinearities activated in other parts of the dendrites, during the propagation of the dendritic spike, or in the soma itself, could boost the effect that dendritic spikes had on the soma membrane potential. Thus, the boost function captured the fact that somatic depolarization due to a dendritic current spike was larger than that predicted by the spike size at the dendrites. It is important to emphasize, however, that the boost function (*B*) did not change the dynamics of I_{NL} but only scaled its magnitude as illustrated in Fig. 8*A* (green vs. purple spikes).

We optimized the soma filter (*G*) and found that it was essentially identical between the two models. The average soma filter (black) was more low pass compared with the dendritic (*D*) and spike filters (*S*) but had a similar peak in its frequency response ~8 Hz (Fig. 8*B*). As shown by the three example filters in Fig. 8*B*, the soma filters became more attenuating, both for amplitude and frequency, as a function of dendritic location. For the linear model of the somatic mem-

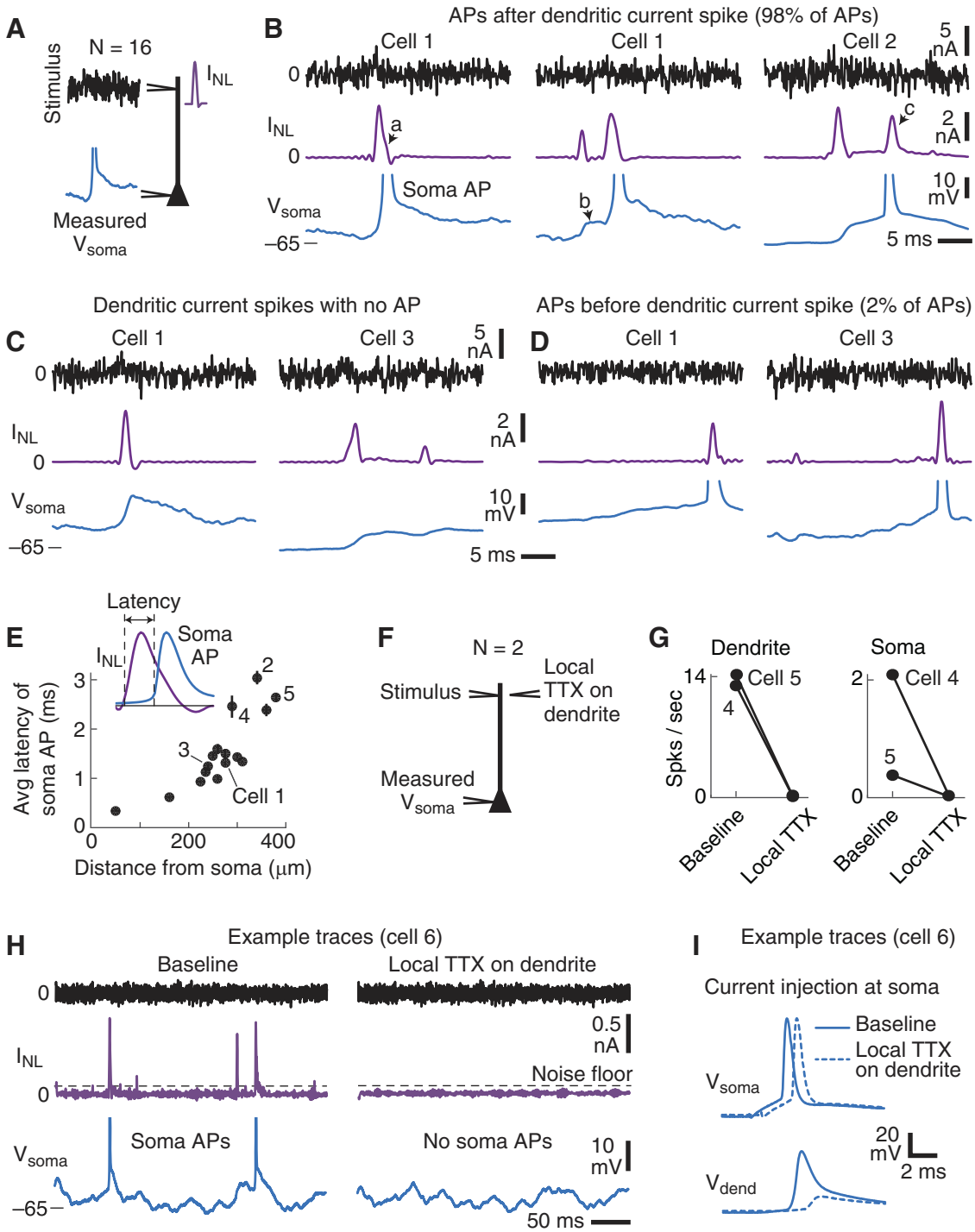

Fig. 7. Dendritic spikes were linked to most somatic APs. *A*: simultaneous dendritic and soma recordings were performed with the large-noise stimulus. *B*: example traces (cells identified in *E*) of the stimulus (black), measured V_{soma} (blue), and I_{NL} (purple). *Left*: a somatic AP that followed a large dendritic current spike. In some cases, the back-propagating APs tended to produce a slight bump that widened the dendritic spike (*arrow a*). *Center*: 2 smaller dendritic current spikes. The first current spike depolarized the somatic potential (*arrow b*), and the second spike was followed by the somatic AP. *Right*: a large dendritic current spike preceded the AP, which was then followed by a second, smaller, dendritic spike (*arrow c*). Across all experiments, ~98% of somatic APs followed a large dendritic current spike. *C*: examples of large dendritic spikes with no somatic AP. *D*: example traces of somatic APs that occurred before large dendritic current spikes. Presumably, these current spikes were the result of back-propagating APs. Only 2% of somatic APs did not follow a dendritic current spike. *E*: the average AP latency (measured from the start of the largest nearby dendritic current spike to the start of the somatic AP; see MATERIALS AND METHODS) increased with the dendritic electrode distance from the soma. Cell numbers correspond to the example traces in other panels. Errors bars are SE. *F*: 2 experiments were performed while TTX was locally applied to the dendritic electrode and large-amplitude noise was injected at the dendrite. *G*: local application of TTX eliminated all dendritic current spikes and somatic APs in response to the noise stimulus injected at the dendrite. *H*: example traces before (*left*) and during (*right*) local TTX application at the dendritic electrode only. *I*: example somatic APs and dendritic potentials in response to current injections at the soma before (solid lines) and during (dashed lines) local TTX application to the dendritic electrode.

brane potential, convolving the somatic filter (G) with the stimulus did a good job of accounting for V_{soma} (yellow, Fig. 8*C*), except for periods after a dendritic current spike.

Including I_{NL} improved the model's ability to mimic the subthreshold soma potential after a dendritic spike. Optimizing the boost function revealed an average increase in the effect that I_{NL} had on the soma potential (Fig. 8*D*). This increase was greater for larger-amplitude dendritic spikes, with an average maximum boost to the dendritic spikes of 40 ± 18% ($P < 0.0001$, $N = 16$, 1-sided t-test). The maximal boosting was not strongly related to dendritic location (Pearson's $R = 0.39$, $P = 0.13$). Example traces of the boosted I_{NL} arriving at the soma filter (G) are shown in Fig. 8*C* (green, *arrow a*), which were smaller than average for this particular neuron.

Importantly, convolving the soma filter (G) with the stimulus + boosted I_{NL} yielded a model V_{soma} (orange traces, Fig. 8*C*) that reproduced the measured somatic membrane potential before and after dendritic spikes (*arrow b*) but not during somatic APs. For example, excluding the 20 ms following the start of a somatic AP (which was ~2% of the data), the linear + I_{NL} model predicted V_{soma} with a median VAF = 99% (range 96–100%, $N = 16$).

To further quantify the interplay between the stimulus, dendritic spikes, and somatic response, we computed population STAs aligned to the start of the dendritic spikes (Fig. 8*E*). We binned dendritic current spikes into three groups: *1*) dendritic spikes that preceded a somatic AP (Fig. 8*E*, *left*), *2*) the largest dendritic spikes with no somatic APs (Fig. 8*E*, *center*), and *3*) the next largest dendritic spikes with no soma AP (Fig. 8*E*, *right*). All three STAs were computed with the same number of dendritic current spikes.

Across 16 experiments, the stimulus STA before a somatic AP (*arrow c*, Fig. 8*E*) revealed the same preferred input dynamics (compare to the STAs in Fig. 4*B*). At the start of an AP, large dendritic current spikes produced a substantial increase in V_{soma} for the linear + I_{NL} model (Fig. 8*E*, orange, *arrow d*), but the model tended to overestimate the somatic depolarization immediately after the AP. This overestimation was likely due to the repolarization of the somatic potential by somatic nonlinearities not captured in the dendritic nonlinearity I_{NL}. In comparison, when there was no somatic AP, the STA of the linear + I_{NL} model of V_{soma} (Fig. 8*E*, orange) overlapped the STA of the measured somatic potential (Fig. 8*E*, *arrows e* and *f*; *insets* show expanded fits). Before the start of the dendritic spike, both models of V_{soma} predicted the somatic membrane potential equally well.

When no somatic AP occurred, the functional model of V_{soma} showed that slightly boosted dendritic spikes were linearly integrated by the soma in a similar manner as the stimulus. The modeling of the somatic potential, however, does not reveal the mechanism by which dendritic spikes were linked to somatic APs. We addressed this next by examining why some large dendritic current spikes did not produce somatic APs, while other large dendritic spikes did produce APs.

Link between dendritic spike and somatic AP depended on stimulus history. Why did some large dendritic current spikes result in somatic APs, while other similarly sized dendritic spikes did not? Previous studies have demonstrated that somatic APs do not always follow dendritic spikes (Gasparini and Magee 2006; Golding and Spruston 1998; Palmer et al. 2014; Sivyer and Williams 2013; Smith et al. 2013; Stuart et al. 1997). We took advantage of the fact that our dendritic spikes varied in amplitude to quantify this link with our functional models of V_{soma}. Figure 9*A* shows the 5–95% range of the dendritic current spike amplitude for our 16 paired recordings as a function of distance from the soma; two groups of spike amplitudes are shown, those that were followed by soma APs (blue) and the largest current spikes not followed by a soma AP (orange). Note that these are the same data used to construct the STAs in Fig. 8*E*, *left* and *center*, and for many experiments there was a substantial overlap in the spike amplitudes between APs and no APs.

Without a somatic AP, there was no systematic relation between dendritic location and the median dendritic spike amplitude (orange, Fig. 9*A*; $R = 0.35$, $P = 0.18$). The median dendritic spike amplitude before an AP, however, was correlated with dendritic location (blue, Fig. 9*A*, $R = -0.75$, $P = 0.008$). The reason for this was that at very proximal dendritic locations the back-propagating AP merged into the dendritic spike and increased its peak amplitude. At more distal locations, the back-propagating AP arrived well after the dendritic current spike peak.

To quantify the link between the dendritic current spike amplitude and soma AP, we matched dendritic spikes with similar peak amplitudes between those followed by a somatic AP and those with no AP. The traces in Fig. 9*B* show examples of two matched dendritic current spikes from the same cell

Fig. 8. A functional model reveals that dendritic spikes were linearly integrated by the soma. *A*: 2 functional models were constructed to describe the somatic membrane response (V_{soma}) to the injection of white-noise current at the dendrite. In the first "linear model" a linear filter (G, referred to as a soma filter) was convolved with the stimulus current to produce V_{soma} (yellow). For the second "linear + I_{NL} model" the stimulus + a boosted I_{NL} (green) was convolved with the same linear filter (G) to produce V_{soma} (orange). The boost to I_{NL} was modeled with a static nonlinearity (B) that simply scaled the I_{NL} amplitude. Note that these models were designed to reproduce the subthreshold fluctuations in V_{soma} (not somatic APs). *B*: average and 3 example linear somatic filters (G). *Top*: mean normalized impulse response function (black). *Inset*: 3 example filters for different dendritic input locations (to compare individual filters, the amplitudes were not normalized; scale bar is 50 ms). *Bottom*: mean normalized impedance amplitude profile (black) and example filters. Soma filters (G) were the same for both soma models shown in *A*. *C*: example traces showing the model fits (same *cell 1* from Fig. 7). For this particular neuron, I_{NL} was only weakly boosted (green vs. purple) before arriving at the soma (*arrow a*). Before a dendritic spike occurred, V_{soma} was well described by the linear filter model (G) convolved with the stimulus (yellow vs. blue). In the presence of dendritic spikes, convolving G with the stimulus + boosted I_{NL} (green) accounted for V_{soma} (orange vs. blue, *arrow b*), except during a somatic AP. *D*: the boosting of I_{NL} arriving at the soma (B) was modeled as a quadratic function. The amount of boosting depended on the dendritic spike amplitude and was on average 40% for the largest dendritic spikes (black). Dashed line is unity slope, and the red, yellow, and blue curves are the single-cell examples corresponding to the recording locations shown in *B*. *E*: population average dendritic spike-triggered averages (STAs) of the stimulus (black), I_{NL} (purple), boosted I_{NL} arriving at the soma (green), and the measured somatic membrane potentials (blue). Also shown are the STAs of the 2 model fits of the somatic membrane potential (yellow and orange). *Left*: STAs using dendritic current spikes that were followed by a somatic AP. *Center*: STAs using the largest dendritic current spikes not associated with a soma AP. *Right*: STAs using the next largest current dendritic spikes not associated with a soma AP. The same total number of dendritic current spikes contributed to each of the 3 STA groups. *Insets* show the average linear + I_{NL} model fit (orange) on a zoomed scale (box is 5 ms × 2 mV). Shading is SE. See main text for arrow references.

with nearly identical amplitudes (I_{NL}; Fig. 9*B*, *middle*). Traces are aligned to the start of the dendritic spikes. Note that the measured somatic potential (solid lines, Fig. 9*B*, *bottom*) at the start of the dendritic spike was more depolarized when a somatic AP occurred (blue vs. orange). Also note that the back-propagating AP substantially widened the dendritic spike (I_{NL}, blue) compared with its matched "no AP" equivalent (orange) but the rise times of both dendritic current spikes were the same.

The short- and long-dashed lines in Fig. 9*B*, *bottom*, are the predicted V_{soma} from the two soma models described above (see Fig. 8*A*). The overlap between the model and measured V_{soma} shows that the linear integration of the stimulus accounted for the difference in soma depolarization at the start of the dendritic spikes. After the start of the dendritic current spike, the soma model that included I_{NL} (long dashes) accurately predicted the soma potential when there was no soma AP (orange, *arrow a*).

Only nine experiments contained enough dendritic spikes of similar size (asterisks in Fig. 9*A*) to perform this comparison, resulting in a total of 617 matched-spike pairs. The population averages (Fig. 9*C*) show that for similar-amplitude dendritic spikes APs occur when the soma potential was more depolarized at the start of the dendritic spike. Importantly, both soma

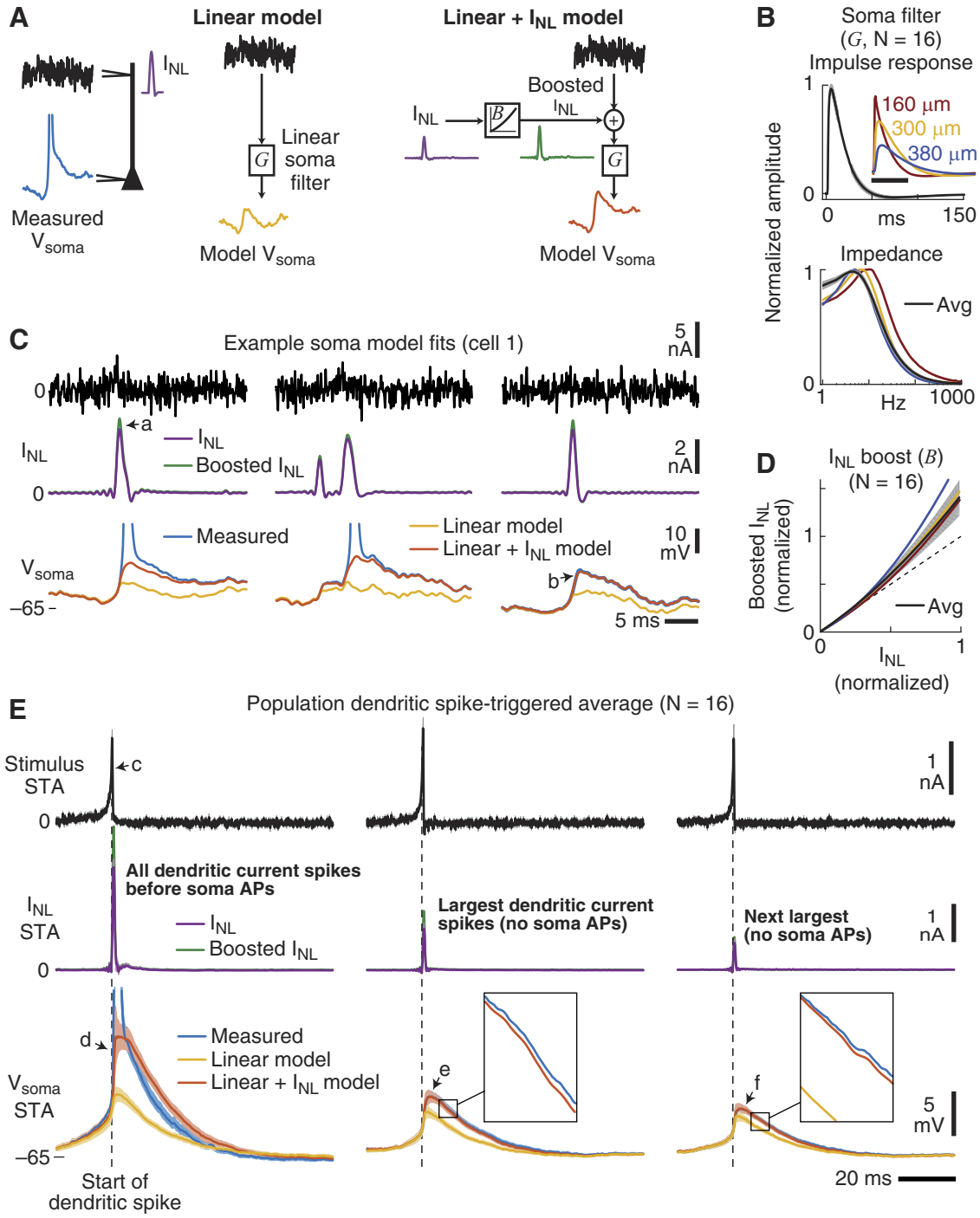

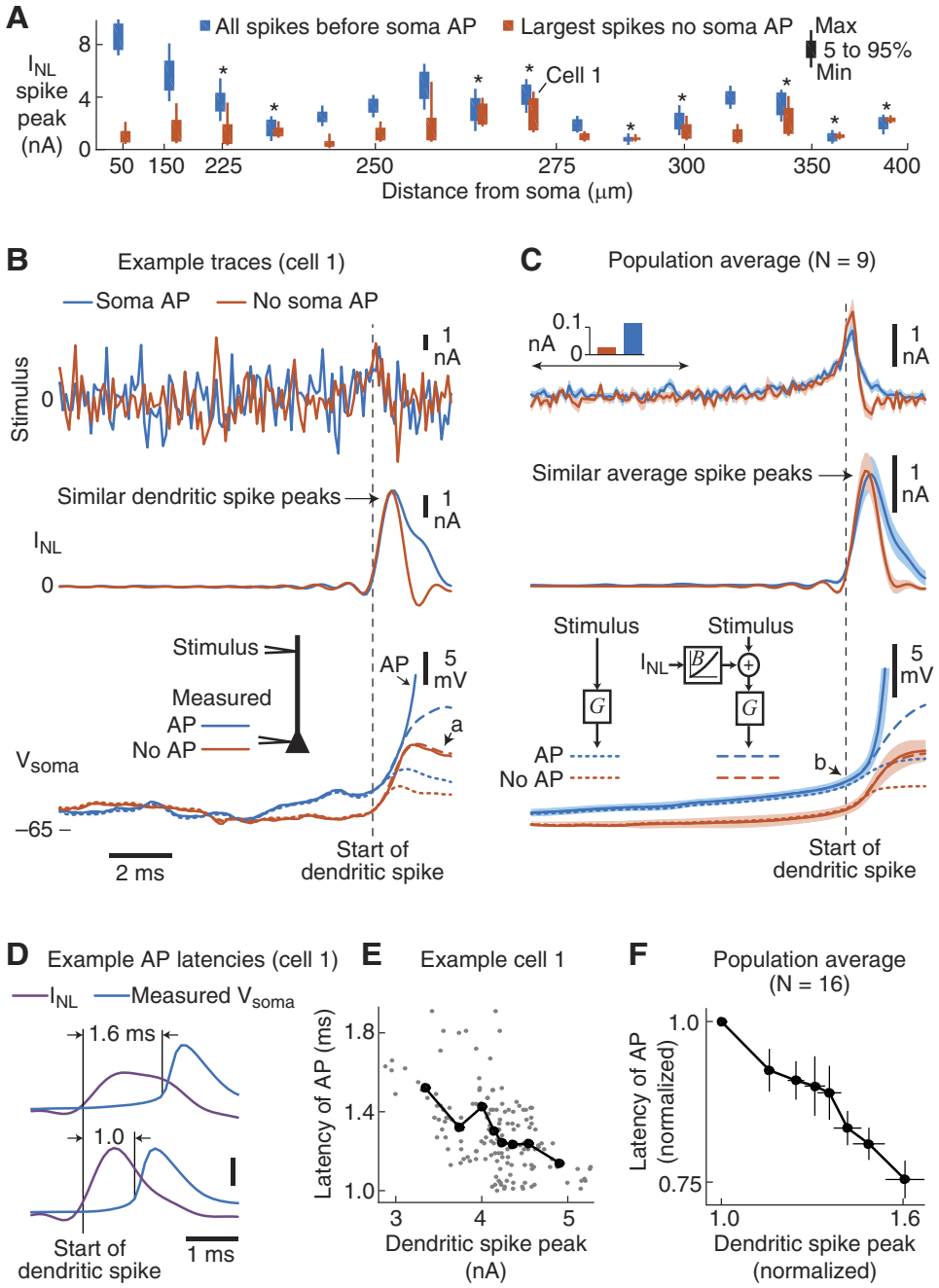

Fig. 9. Link between dendritic current spikes and somatic APs is modulated by the stimulus history. *A*: range of dendritic current spike amplitude vs. the distance of the dendritic electrode from the soma. Each box represents the 5–95% range, and vertical lines are min to max. Dendritic current spikes were grouped by those that were followed by somatic APs (blue) and those that were not (orange). The dendritic current spikes for this plot are the same as those that comprised the population STAs in Fig. 8*E*, *left* and *center*. Asterisks indicate experiments where there was enough overlap between the 2 groups to match similar-sized dendritic current spikes. *B*: example traces for the stimulus, I_{NL}, and V_{soma} for 2 similar-sized dendritic current spikes where one was followed by a somatic AP (blue) while the other was not (orange). Alignment is to the start of the dendritic spike (vertical dashed line). Note the bump in the falling phase of the dendritic current spike (blue), presumably due to AP back-propagation. The output of the 2 functional soma models reproduced V_{soma} until the start of the dendritic spike. The soma filter (G) was convolved with either the stimulus (short-dashed lines) or the stimulus + boosted I_{NL} (long-dashed lines). *Cell 1* is the same as in Figs. 7 and 8. *Arrow a* indicates the good fit of the stimulus + boosted I_{NL} model following a dendritic current spike. *C*: population averages of the STAs for similar-sized dendritic current spikes. Of our 16 dual recordings, 9 locations had at least 20 similar-sized dendritic current spikes to allow a comparison (asterisks in *A*), for a total of 617 dendritic spike pairs. All neurons demonstrated a depolarized V_{soma} at the start of the dendritic spike when an AP occurred compared with when an AP did not follow the dendritic spike. Both functional models of V_{soma} predicted the depolarized soma potential before an AP (note that the population STA of the model that included I_{NL} perfectly overlapped V_{soma} before the start of the dendritic spike, *arrow b*). *Inset* in *top* panel is the average stimulus current for the 5-ms range shown and highlights that the past stimulus was larger before an AP. Shading is SE. *D*: examples of a short (1 ms) and a long (1.6 ms) latency between the start of the dendritic current spike and the start of the soma AP. Vertical scale bar is 2 nA and 40 mV. *E*: AP latency vs. dendritic spike amplitude for all APs in an example recording (small gray points). Latency and spike amplitudes were averaged in 8 equal-sized bins (large black points). *F*: the population average of the binned latency was linearly related to the binned peak dendritic spike amplitude. Each cell was normalized to the smallest amplitude current spikes before averaging. Error bars are SE.

models mimicked this observation, with the model that included I_{NL} (long dashes) perfectly overlapping the average measured V_{soma} at the time of the dendritic spike (Fig. 9*C*, blue, *arrow b*). Because the soma has a long integration period (as shown by the soma filter *G* in Fig. 8*B*), small differences in past dendritic inputs were linearly accumulated and directly influenced the neuron's decision to produce an AP. The small bar plot in Fig. 9*C*, *top*, highlights that the average stimulus 5–10 ms before the dendritic spike was greater and thus more depolarizing for somatic APs (blue) vs. no APs (orange).

These results suggest that the somatic integration had a strong effect on the link between dendritic current spikes and somatic APs. The functional models show that because the soma integrates over a relatively long window both the stimulus and dendritic spike history contribute to the neuron's decision to produce an AP. Thus, some large dendritic spikes were not followed by APs when they were combined with a weakly depolarizing stimulus history.

Dendritic spike amplitude contributed to latency of somatic AP. The latency from the start of the dendritic spike (I_{NL}) to the start of the somatic AP varied within each cell (examples of a short and a long AP latency are shown in Fig. 9*D*). Furthermore, the variability in AP latency was correlated with the amplitude of the dendritic current spike. Figure 9*E* shows AP latencies from the same example cell as a function of the preceding dendritic spike peak (gray points).

Across all 16 experiments, the average Pearson's correlation between dendritic spike peak and AP latency was -0.38 ± 0.05 ($P < 0.0001$, *t*-test). To illustrate this relationship, we binned the peak amplitude of the dendritic spike and the AP latency into eight equal-sized groups (large black points, Fig. 9*E*). The population average revealed a nearly linear relationship between binned dendritic spike amplitude and AP latency (Fig. 9*F*), with a ~60% increase in dendritic current spike amplitude corresponding to a ~25% reduction in AP latency.

The relationship shown in Fig. 9*F* is consistent with the linear integration of dendritic spikes until an AP threshold is reached. In other words, larger dendritic spikes produced slightly faster charging curves of the soma (and presumably axon) membrane potential. If dendritic spikes had an all-or-none effect on the AP, then we would expect little correlation between latency and dendritic spike amplitude.

In summary, the functional modeling of V_{soma}, matching dendritic spikes with and without APs, and the latency results together suggest that the decision to produce an AP was not just an all-or-none regenerative event triggered by large dendritic spikes. Instead, the somatic integration of the combined dendritic current spikes and stimulus was a significant factor for the production and timing of somatic APs.

Somatic APs were selective to same stimulus preferred by dendrites. During the large white-noise stimulus, large-amplitude dendritic spikes preceded APs ~98% of the time, suggesting that soma APs would also be selective to the same stimulus features preferred by the dendrite. In five experiments we injected the same stimulus patterns used to measure the selectivity of I_{NL} (see Fig. 6) while simultaneously monitoring the somatic and dendritic potentials (Fig. 10*A*). As highlighted by the example traces in Fig. 10*B*, somatic APs usually occurred after a large dendritic spike for both the signal-only and signal+noise conditions (Fig. 10*B*, *left* and *right*, respectively).

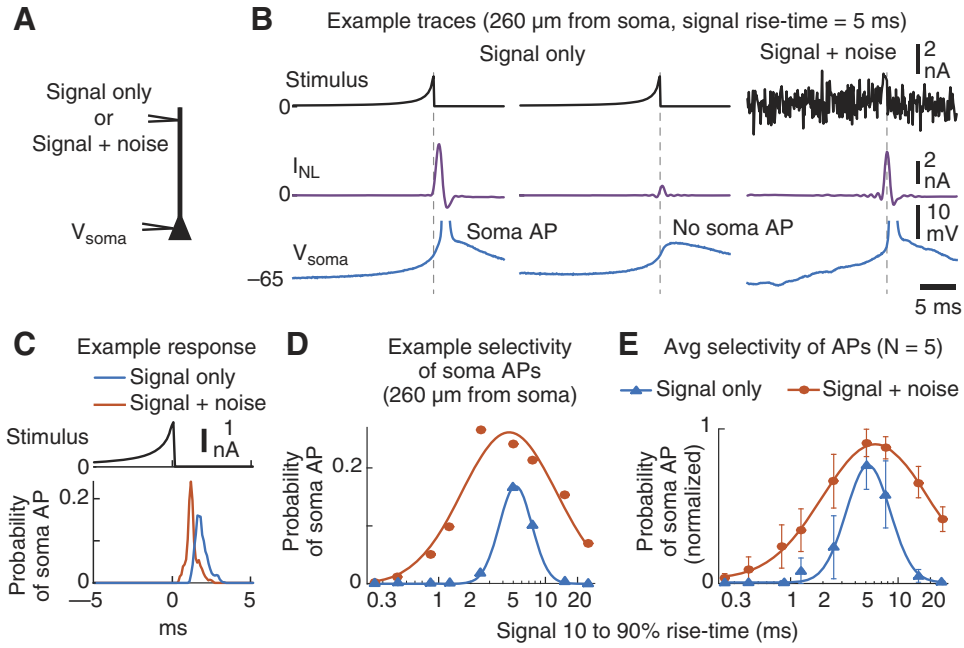

Fig. 10. Somatic APs were selective to the same temporal input feature as that of the dendritic spikes. *A*: dendritic and somatic membrane potentials were measured simultaneously in response to the signal-only and signal+noise conditions shown in Fig. 6. *B*: example traces in response to the same 5-ms rise time signal. *Left*: a large dendritic current spike and soma AP that followed the preferred signal waveform. *Center*: a small dendritic current spike and failed AP in response to the preferred signal. *Right*: a soma AP followed a dendritic spike when the preferred signal was presented in the presence of noise. Vertical dashed line indicates the end of the signal. *C*: example of the probability of a somatic AP occurring in response to the preferred (5-ms rise time) signal only (blue) and signal+noise (orange). Peak probabilities were computed for each of the 9 signal waveforms. Data are from the same neuron in *B*. *D* and *E*: example (*D*) and average normalized probability (*E*) of a somatic AP in response to the signal-only (blue) and signal+noise (orange) current injections. Solid lines are Gaussian fits. The selectivity of somatic APs was narrower for the signal-only condition and mirrored the selectivity for dendritic spikes shown in Fig. 6. Error bars are SE.

Also illustrated is an example of a small dendritic current spike and failed somatic AP (Fig. 10*B*, *center*) to the same input signal.

For the signal-only and signal+noise conditions, respectively, somatic AP firing rates were 1.1 ± 1.3 (SD) and 3.6 ± 1.6 spikes/s ($N = 5$), and we recorded a total of 1,539 and 4,706 individual somatic APs. Dendritic spikes preceded ~99% of somatic APs for both conditions. The dendritic location for these recordings ranged from 160 to 300 μm (median 260 μm).

To estimate the selectivity of the somatic APs, we first computed the probability of observing a somatic AP following each signal rise time in our two conditions. For example, the probability of observing a somatic AP following the 5 ms rise time signal is shown for a single cell in Fig. 10*C* and was higher for the signal+noise condition (orange) than the signal-only condition (blue). Plotting the peak probability of an AP vs. the signal 10–90% rise time revealed Gaussian selectivity of the somatic APs (Fig. 10, *D* and *E*). The preferred selectivity of somatic APs was similar to that of the dendritic current spikes (compare to Fig. 6*G*). For example, the selectivity of the somatic APs was narrower for the signal-only condition than the signal+noise condition. These results demonstrate that the output of a neuron is shaped by the selectivity of the nonlinear dendritic signal processing.

DISCUSSION

For the subtype of mouse L5 neurons explored here (PT neurons), we have provided evidence that both fast dendritic spikes and somatic APs are selective to the same dynamical feature of the dendritic input. Thus, the dendritic spike amplitude conveyed information to the neuron about the shape of the stimulus and influenced the occurrence of APs. The white-noise stimulus produced a high rate of dendritic spikes of varying amplitudes, while APs occurred at a much lower rate. Dendritic current injections of individual waveforms (signal-only and signal+noise conditions) corroborated the results obtained from the noise injections.

A functional model accurately captured the amplitude and timing of individual dendritic spikes in response to noise and individual waveforms and predicted the selectivity of the dendritic spikes for the waveform inputs. Importantly, the functional model of the dendritic spikes accounted for how the selectivity broadened when noise was added to the input (signal+noise condition). A second functional model of the somatic response suggested that boosted dendritic spikes are combined with the stimulus over the soma's relatively long integration window. However, the source of the boosting was not measured and could have resulted from the contribution of nonlinearities in other parts of the dendrites or soma, or during the propagation of the dendritic spike to the soma.

Our current injections bypassed the synaptic conductance, which could affect the linear component of the dendrite (Destexhe and Paré 1999) or add additional nonlinearities such as NMDA spikes (Larkum et al. 2009; Palmer et al. 2014). In addition to being a useful tool in systems identification, our noise stimulus may have captured the highly variable input that dendrites receive in vivo. For example, assuming that cortical neurons fire at a low background rate of 1 spike/s, there would be ~10,000 EPSCs per second bombarding a typical dendritic tree. Furthermore, in vivo intracellular recordings typically show fast fluctuations in the somatic potential during normal cortical circuit function (Destexhe et al. 2003; Smith et al. 2013). Because we adjusted our stimulus amplitudes at the dendrites to produce low firing in order to study somatic APs in isolation (Agüera y Arcas and Fairhall 2003), we may not have revealed the full range of dendritic nonlinearities. For example, PFC neurons typically have in vivo background firing rates of 5–10 spikes/s (Wang et al. 2011), while our signal+noise condition produced our highest AP firing of ~4 spikes/s. Another difference is that while AP bursts are common in some pyramidal neurons, bursts were associated with only 15% of somatic APs in our recordings.

Our results are consistent with a rich body of evidence that in many neurons there are multiple integration zones (Das and Narayanan 2014, 2015; Gasparini and Magee 2006; Larkum et al. 2009; Poirazi et al. 2003a, 2003b; Sivyer and Williams 2013; Smith et al. 2013). Local input features are extracted by dendritic nonlinearities, with the results integrated at the soma. Dendritic nonlinearities in the form of Ca^{2+} plateau potentials and Na^{+} spikes have been observed in several types of pyramidal neurons across many brain regions (Harnett et al. 2013; Larkum et al. 1999a, 1999b; Schiller et al. 1997, 2000; Stuart et al. 1997; Stuart and Spruston 2015; Takahashi and Magee 2009; Xu et al. 2012). These dendritic spikes are capable of triggering somatic APs and can improve the temporal precision of AP output (Ariav et al. 2003), yet the relative contribution of linear vs. nonlinear dendritic processing to somatic APs has been unclear. A major advantage of the systems modeling approach used here is that we were able to isolate the nonlinear component of the dendrites during arbitrary dendritic inputs.

Our systems-based results agree with biophysical models that suggest that spike-generating mechanisms in the dendrites can modulate the dynamics of APs measured at the soma (Das and Narayanan 2014, 2015; Poirazi et al. 2003a, 2003b). Consequently, high-frequency inputs that are preferred by the dendrites produce spikes, which are subsequently integrated linearly at the soma. While our data clearly show subthreshold linear integration of dendritic spikes at the soma, we could not conclusively demonstrate that this was the sole factor in determining AP initiation in the axon. Regardless of the mechanism, however, under both our noise and nonnoise input conditions, AP generation was selective to the same preferred input dynamics as the dendrites. The opposite did not hold, as the occurrence of a large nonlinear dendritic spike did not guarantee a somatic AP.

Our results apply specifically to fast dendritic Na^{+} spikes in PT neurons of PFC. Other sources of dendritic and synaptic nonlinearities (especially NMDA spikes) can profoundly affect AP generation (Harnett et al. 2013; Larkum et al. 1999a, 1999b, 2009; Palmer et al. 2014; Schiller et al. 2000; Stuart and Spruston 2015; Takahashi and Magee 2009; Xu et al. 2012). Notably, these other sources of nonlinearities are also capable of producing dendritic Na^{+} spikes, suggesting that dendritic nonlinearities interact in ways not captured by our noise current injections.

The properties of our three stimulus types (noise only, signal only, and signal+noise) may have biased our neurons to mainly produce APs following dendritic spikes. Although the Poisson-like firing statistics observed in cortical neurons (Goris et al. 2014) would likely produce highly random fluctuations in

dendrites, our stimuli lacked certain features of the up/down states observed in vivo (Destexhe et al. 2003; Williams 2005). For example, other input dynamics tend to produce a more variable relationship between dendritic spike and AP (Gasparini and Magee 2006; Golding and Spruston 1998; Palmer et al. 2014; Sivyer and Williams 2013; Smith et al. 2013; Stuart et al. 1997). However, the presence of the same nonlinear dendritic spikes in our three different stimuli suggests that our selectivity results were not overly dependent on the statistical structure of the input.

It is also possible that Na^+ spikes are the predominant type of dendritic nonlinearity in PT neurons of PFC. Our recording locations were centered on the nexus of the apical dendrite, a location where Ca^{2+} electrogenesis has been reported to have a low threshold in L5 neurons of sensory cortices (Larkum et al. 1999b; Larkum and Zhu 2002). Our results are thus consistent with previous reports that the apical dendrite of L5 neurons of PFC display little Ca^{2+} electrogenesis compared with L5 neurons from primary sensory cortices (Gulledge and Stuart 2003; Santello and Nevian 2015). It remains possible, however, that Ca^{2+} electrogenesis occurs at different locations, for example, in the distal apical tuft regions of PT neurons of PFC. The novel deconvolution method outlined here, however, could be used to quantify how the full repertoire of dendritic nonlinearities regulates somatic AP generation. Although infrequent, we observed sustained inward nonlinearities lasting longer than 10 ms. Similarly, our method could be used to examine how the presence of synaptic nonlinearities (Larkum et al. 2009; Palmer et al. 2014; Polsky et al. 2004; Schiller et al. 2000; Smith et al. 2013) or the occurrence of different network states (Destexhe et al. 2003; Destexhe and Paré 1999) affects the interplay between linear and nonlinear dendritic processing and AP generation.

Dendritic selectivity and variable-amplitude Na^+ spikes. Variable-amplitude dendritic nonlinearities have been observed previously (Golding and Spruston 1998; Sivyer and Williams 2013; Smith et al. 2013). For example, Sivyer and Williams (2013) showed that in retinal ganglion cells small-amplitude spikes were initiated at locations distal to the recording location, integrated at parent dendrites to produce subsequent dendritic spikes and eventually somatic APs. A similar integration of dendritic Na^+ spikes originating at separate dendritic branches may occur in L5 neurons. While the smaller-amplitude spikes we recorded did not usually elicit APs, they nonetheless contributed to the depolarization at the soma. This conclusion is supported by the fact that integrating the sum of the stimulus and boosted dendritic spikes accounted for ~99% of the variability in the somatic membrane potential. These smaller-amplitude Na^+ spikes can summate to elicit somatic APs (e.g., Fig. 7*B*). Given the theta resonance of the dendrite, trains of small-amplitude dendritic spikes in the theta frequency range would be predicted to preferentially elicit a somatic AP.

Our results are the first, to our knowledge, to quantitatively link the dendritic spike amplitude and soma AP to a specific shape of the dendritic input. However, previous studies have demonstrated that the probability of dendritic spike generation depends on the temporal and spatial properties of the synaptic input (Branco et al. 2010; Branco and Häusser 2011; Gasparini et al. 2004; Gasparini and Magee 2006). While our data do not address the spatial selectivity of dendritic nonlinearities or how the spatial profile of dendritic input affects dendritic nonlinearities, they do suggest that the temporal dynamics of the dendritic input contribute significantly to the variability in dendritic spike size.

Functional considerations. Temporal synchrony in the activity of subsets of neurons plays a key role in several aspects of brain function and cognition (Engel et al. 2001) including attention, motor movement planning, sensory processing, and working memory (Fries et al. 2001b; Riehle et al. 1997; Steinmetz et al. 2000; Yamamoto et al. 2014). Temporally coordinated spiking propagates to downstream networks of neurons (Reyes 2003; Zandvakili and Kohn 2015), and synchronous synaptic inputs are capable of entraining the spiking activity of pyramidal neurons (Colgin et al. 2009; Fries et al. 2001a).

While temporal synchrony plays a key role in brain function, it presents an apparent paradox when considering how neurons process high-frequency synaptic inputs. Specifically, the high-frequency components contained in synchronous inputs are largely removed by the long integration time of the dendrite-to-soma filter (Cook et al. 2007; Dembrow et al. 2015; Softky and Koch 1993; Vaidya and Johnston 2013). A potential solution to this conundrum is that dendritic nonlinearities become engaged during specific high-frequency synchronous inputs. The selectivity of these nonlinearities could differ between neurons or even within a single neuron at different dendritic locations. In the case of our L5 PT neurons in PFC, the selectivity of dendritic spikes to rise times between 2 and 6 ms (Fig. 6*H*) would facilitate locking of APs to input arriving at gamma frequency ranges or even higher. Similarly, differences in selectivity of dendritic spikes across the dendritic axis could explain how different frequencies of gamma oscillations arriving at different dendritic locations are capable of entraining AP firing in CA1 pyramidal neurons (Colgin et al. 2009; Das and Narayanan 2014, 2015). For example, the selectivity of nonlinearities at distal dendritic locations might facilitate fast gamma (~80 Hz) entrainment of APs, whereas at proximal locations a different selectivity window might facilitate slow gamma entrainment of AP firing (~40 Hz).

Our functional model, in which high-frequency input features are extracted by the spike filter (*S*), rectified by the nonlinearity (*Z*), and then low-passed at the soma (*G*), has notable parallels to models that extract information contained in the amplitude-modulated envelope of high-frequency carriers (Baker 1999; Clarke et al. 2015). Thus, our results provide insights into the cellular mechanisms that allow the envelope of high-frequency synchronous inputs to preferentially entrain somatic APs despite the low-pass filtering properties of the dendrite.

ACKNOWLEDGMENTS

We thank Randy Chitwood and Darrin Brager for the cell image in Fig. 1.

Present address of B. E. Kalmbach: Allen Institute for Brain Science, Seattle, WA 98109.

GRANTS

This work was supported by National Institutes of Health Grants R01 MH-094839 (D. Johnston), NS-084473 (D. Johnston), and F32 MH-090694 (B. E. Kalmbach) and Natural Sciences and Engineering Research Council Grant RGPIN 326804-12 (E. P. Cook).

DISCLOSURES

No conflicts of interest, financial or otherwise, are declared by the author(s).

AUTHOR CONTRIBUTIONS

B.E.K., R.G., D.J., and E.P.C. conceived and designed research; B.E.K. and R.G. performed experiments; B.E.K. and E.P.C. analyzed data; B.E.K., R.G., D.J., and E.P.C. interpreted results of experiments; B.E.K. and E.P.C. prepared figures; B.E.K. and E.P.C. drafted manuscript; B.E.K., R.G., D.J., and E.P.C. edited and revised manuscript; B.E.K., R.G., D.J., and E.P.C. approved final version of manuscript.

REFERENCES

Aqüera y Arcas B, Fairhall AL. What causes a neuron to spike? *Neural Comput* 15: 1789–1807, 2003. doi:10.1162/08997660360675044.

Ariav G, Polsky A, Schiller J. Submillisecond precision of the input-output transformation function mediated by fast sodium dendritic spikes in basal dendrites of CA1 pyramidal neurons. *J Neurosci* 23: 7750–7758, 2003.

Baker CL Jr. Central neural mechanisms for detecting second-order motion. *Curr Opin Neurobiol* 9: 461–466, 1999. doi:10.1016/S0959-4388(99)80069-5.

Bean BP. The action potential in mammalian central neurons. *Nat Rev Neurosci* 8: 451–465, 2007. doi:10.1038/nrn2148.

Branco T, Clark BA, Häusser M. Dendritic discrimination of temporal input sequences in cortical neurons. *Science* 329: 1671–1675, 2010. doi:10.1126/science.1189664.

Branco T, Häusser M. Synaptic integration gradients in single cortical pyramidal cell dendrites. *Neuron* 69: 885–892, 2011. doi:10.1016/j.neuron.2011.02.006.

Bryant HL, Segundo JP. Spike initiation by transmembrane current: a white-noise analysis. *J Physiol* 260: 279–314, 1976. doi:10.1113/jphysiol.1976.sp011516.

Clarke SE, Longtin A, Maler L. Contrast coding in the electrosensory system: parallels with visual computation. *Nat Rev Neurosci* 16: 733–744, 2015. doi:10.1038/nrn4037.

Colgin LL, Denninger T, Fyhn M, Hafting T, Bonnevie T, Jensen O, Moser MB, Moser EI. Frequency of gamma oscillations routes flow of information in the hippocampus. *Nature* 462: 353–357, 2009. doi:10.1038/nature08573.

Cook EP, Guest JA, Liang Y, Masse NY, Colbert CM. Dendrite-to-soma input/output function of continuous time-varying signals in hippocampal CA1 pyramidal neurons. *J Neurophysiol* 98: 2943–2955, 2007. doi:10.1152/jn.00414.2007.

Das A, Narayanan R. Active dendrites regulate spectral selectivity in location-dependent spike initiation dynamics of hippocampal model neurons. *J Neurosci* 34: 1195–1211, 2014. doi:10.1523/JNEUROSCI.3203-13.2014.

Das A, Narayanan R. Active dendrites mediate stratified gamma-range coincidence detection in hippocampal model neurons. *J Physiol* 593: 3549–3576, 2015. doi:10.1113/JP270688.

de Boer R, Kuyper P. Triggered correlation. *IEEE Trans Biomed Eng* 15: 169–179, 1968. doi:10.1109/TBME.1968.4502561.

Dembrow NC, Chitwood RA, Johnston D. Projection-specific neuromodulation of medial prefrontal cortex neurons. *J Neurosci* 30: 16922–16937, 2010. doi:10.1523/JNEUROSCI.3644-10.2010.

Dembrow NC, Zemelman BV, Johnston D. Temporal dynamics of L5 dendrites in medial prefrontal cortex regulate integration versus coincidence detection of afferent inputs. *J Neurosci* 35: 4501–4514, 2015. doi:10.1523/JNEUROSCI.4673-14.2015.

Destexhe A, Paré D. Impact of network activity on the integrative properties of neocortical pyramidal neurons in vivo. *J Neurophysiol* 81: 1531–1547, 1999.

Destexhe A, Rudolph M, Paré D. The high-conductance state of neocortical neurons in vivo. *Nat Rev Neurosci* 4: 739–751, 2003. doi:10.1038/nrn1198.

Engel AK, Fries P, Singer W. Dynamic predictions: oscillations and synchrony in top-down processing. *Nat Rev Neurosci* 2: 704–716, 2001. doi:10.1038/35094565.

Fries P. Neuronal gamma-band synchronization as a fundamental process in cortical computation. *Annu Rev Neurosci* 32: 209–224, 2009. doi:10.1146/annurev.neuro.051508.135603.

Fries P, Neuenschwander S, Engel AK, Goebel R, Singer W. Rapid feature selective neuronal synchronization through correlated latency shifting. *Nat Neurosci* 4: 194–200, 2001a. doi:10.1038/84032.

Fries P, Reynolds JH, Rorie AE, Desimone R. Modulation of oscillatory neuronal synchronization by selective visual attention. *Science* 291: 1560–1563, 2001b. doi:10.1126/science.1055465.

Gasparini S, Magee JC. State-dependent dendritic computation in hippocampal CA1 pyramidal neurons. *J Neurosci* 26: 2088–2100, 2006. doi:10.1523/JNEUROSCI.4428-05.2006.

Gasparini S, Migliore M, Magee JC. On the initiation and propagation of dendritic spikes in CA1 pyramidal neurons. *J Neurosci* 24: 11046–11056, 2004. doi:10.1523/JNEUROSCI.2520-04.2004.

Golding NL, Spruston N. Dendritic sodium spikes are variable triggers of axonal action potentials in hippocampal CA1 pyramidal neurons. *Neuron* 21: 1189–1200, 1998. doi:10.1016/S0896-6273(00)80635-2.

Goris RL, Movshon JA, Simoncelli EP. Partitioning neuronal variability. *Nat Neurosci* 17: 858–865, 2014. doi:10.1038/nn.3711.

Gulledge AT, Stuart GJ. Action potential initiation and propagation in layer 5 pyramidal neurons of the rat prefrontal cortex: absence of dopamine modulation. *J Neurosci* 23: 11363–11372, 2003.

Harnett MT, Xu NL, Magee JC, Williams SR. Potassium channels control the interaction between active dendritic integration compartments in layer 5 cortical pyramidal neurons. *Neuron* 79: 516–529, 2013. doi:10.1016/j.neuron.2013.06.005.

Hu H, Vervaeke K, Graham LJ, Storm JF. Complementary theta resonance filtering by two spatially segregated mechanisms in CA1 hippocampal pyramidal neurons. *J Neurosci* 29: 14472–14483, 2009. doi:10.1523/JNEUROSCI.0187-09.2009.

Hunter IW, Korenberg MJ. The identification of nonlinear biological systems: Wiener and Hammerstein cascade models. *Biol Cybern* 55: 135–144, 1986.

Kalmbach BE, Chitwood RA, Dembrow NC, Johnston D. Dendritic generation of mGluR-mediated slow afterdepolarization in layer 5 neurons of prefrontal cortex. *J Neurosci* 33: 13518–13532, 2013. doi:10.1523/JNEUROSCI.2018-13.2013.

Kalmbach BE, Johnston D, Brager DH. Cell-type specific channelopathies in the prefrontal cortex of the *fmr1-/y* mouse model of fragile X syndrome. *eNeuro* 2: ENEURO.0114-15, 2015. doi:10.1523/ENEURO.0114-15.2015.

Kress GJ, Mennerick S. Action potential initiation and propagation: upstream influences on neurotransmission. *Neuroscience* 158: 211–222, 2009. doi:10.1016/j.neuroscience.2008.03.021.

Larkum ME, Kaiser KM, Sakmann B. Calcium electrogenesis in distal apical dendrites of layer 5 pyramidal cells at a critical frequency of back-propagating action potentials. *Proc Natl Acad Sci USA* 96: 14600–14604, 1999a. doi:10.1073/pnas.96.25.14600.

Larkum ME, Nevian T, Sandler M, Polsky A, Schiller J. Synaptic integration in tuft dendrites of layer 5 pyramidal neurons: a new unifying principle. *Science* 325: 756–760, 2009. doi:10.1126/science.1171958.

Larkum ME, Zhu JJ. Signaling of layer 1 and whisker-evoked Ca^{2+} and Na^{+} action potentials in distal and terminal dendrites of rat neocortical pyramidal neurons in vitro and in vivo. *J Neurosci* 22: 6991–7005, 2002.

Larkum ME, Zhu JJ, Sakmann B. A new cellular mechanism for coupling inputs arriving at different cortical layers. *Nature* 398: 338–341, 1999b. doi:10.1038/18686.

Lathi BP, Ding Z. *Modern Digital and Analog Communication Systems*. New York: Oxford Univ. Press, 2010.

Narayanan R, Johnston D. Long-term potentiation in rat hippocampal neurons is accompanied by spatially widespread changes in intrinsic oscillatory dynamics and excitability. *Neuron* 56: 1061–1075, 2007. doi:10.1016/j.neuron.2007.10.033.

Nettleton JS, Spain WJ. Linear to supralinear summation of AMPA-mediated EPSPs in neocortical pyramidal neurons. *J Neurophysiol* 83: 3310–3322, 2000.

Oviedo H, Reyes AD. Boosting of neuronal firing evoked with asynchronous and synchronous inputs to the dendrite. *Nat Neurosci* 5: 261–266, 2002. doi:10.1038/nn807.

Palmer LM, Shai AS, Reeve JE, Anderson HL, Paulsen O, Larkum ME. NMDA spikes enhance action potential generation during sensory input. *Nat Neurosci* 17: 383–390, 2014. doi:10.1038/nn.3646.

Paninski L. Maximum likelihood estimation of cascade point-process neural encoding models. *Network* 15: 243–262, 2004. doi:10.1088/0954-898X_15_4_002.

Poirazi P, Brannon T, Mel BW. Arithmetic of subthreshold synaptic summation in a model CA1 pyramidal cell. *Neuron* 37: 977–987, 2003a. doi:10.1016/S0896-6273(03)00148-X.

Poirazi P, Brannon T, Mel BW. Pyramidal neuron as two-layer neural network. *Neuron* 37: 989–999, 2003b. doi:10.1016/S0896-6273(03)00149-1.

Polsky A, Mel BW, Schiller J. Computational subunits in thin dendrites of pyramidal cells. *Nat Neurosci* 7: 621–627, 2004. doi:10.1038/nn1253.

Reyes AD. Synchrony-dependent propagation of firing rate in iteratively constructed networks in vitro. *Nat Neurosci* 6: 593–599, 2003. doi:10.1038/nn1056.

Riehle A, Grün S, Diesmann M, Aertsen A. Spike synchronization and rate modulation differentially involved in motor cortical function. *Science* 278: 1950–1953, 1997. doi:10.1126/science.278.5345.1950.

Sakai HM. White-noise analysis in neurophysiology. *Physiol Rev* 72: 491–505, 1992.

Santello M, Nevian T. Dysfunction of cortical dendritic integration in neuropathic pain reversed by serotoninergic neuromodulation. *Neuron* 86: 233–246, 2015. doi:10.1016/j.neuron.2015.03.003.

Schiller J, Major G, Koester HJ, Schiller Y. NMDA spikes in basal dendrites of cortical pyramidal neurons. *Nature* 404: 285–289, 2000. doi:10.1038/35005094.

Schiller J, Schiller Y, Stuart G, Sakmann B. Calcium action potentials restricted to distal apical dendrites of rat neocortical pyramidal neurons. *J Physiol* 505: 605–616, 1997. doi:10.1111/j.1469-7793.1997.605ba.x.

Sivyer B, Williams SR. Direction selectivity is computed by active dendritic integration in retinal ganglion cells. *Nat Neurosci* 16: 1848–1856, 2013. doi:10.1038/nn.3565.

Smith SL, Smith IT, Branco T, Häusser M. Dendritic spikes enhance stimulus selectivity in cortical neurons in vivo. *Nature* 503: 115–120, 2013. doi:10.1038/nature12600.

Softky WR, Koch C. The highly irregular firing of cortical cells is inconsistent with temporal integration of random EPSPs. *J Neurosci* 13: 334–350, 1993.

Steinmetz PN, Roy A, Fitzgerald PJ, Hsiao SS, Johnson KO, Niebur E. Attention modulates synchronized neuronal firing in primate somatosensory cortex. *Nature* 404: 187–190, 2000. doi:10.1038/35004588.

Stuart G, Schiller J, Sakmann B. Action potential initiation and propagation in rat neocortical pyramidal neurons. *J Physiol* 505: 617–632, 1997. doi:10.1111/j.1469-7793.1997.617ba.x.

Stuart GJ, Spruston N. Dendritic integration: 60 years of progress. *Nat Neurosci* 18: 1713–1721, 2015. doi:10.1038/nn.4157.

Takahashi H, Magee JC. Pathway interactions and synaptic plasticity in the dendritic tuft regions of CA1 pyramidal neurons. *Neuron* 62: 102–111, 2009. doi:10.1016/j.neuron.2009.03.007.

Ulrich D. Dendritic resonance in rat neocortical pyramidal cells. *J Neurophysiol* 87: 2753–2759, 2002.

Vaidya SP, Johnston D. Temporal synchrony and gamma-to-theta power conversion in the dendrites of CA1 pyramidal neurons. *Nat Neurosci* 16: 1812–1820, 2013. doi:10.1038/nn.3562.

Wang M, Gamo NJ, Yang Y, Jin LE, Wang XJ, Laubach M, Mazer JA, Lee D, Arnsten AF. Neuronal basis of age-related working memory decline. *Nature* 476: 210–213, 2011. doi:10.1038/nature10243.

Watanabe H, Tsubokawa H, Tsukada M, Aihara T. Frequency-dependent signal processing in apical dendrites of hippocampal CA1 pyramidal cells. *Neuroscience* 278: 194–210, 2014. doi:10.1016/j.neuroscience.2014.07.069.

Williams SR. Encoding and decoding of dendritic excitation during active states in pyramidal neurons. *J Neurosci* 25: 5894–5902, 2005. doi:10.1523/JNEUROSCI.0502-05.2005.

Wu MC, David SV, Gallant JL. Complete functional characterization of sensory neurons by system identification. *Annu Rev Neurosci* 29: 477–505, 2006. doi:10.1146/annurev.neuro.29.051605.113024.

Xu NL, Harnett MT, Williams SR, Huber D, O'Connor DH, Svoboda K, Magee JC. Nonlinear dendritic integration of sensory and motor input during an active sensing task. *Nature* 492: 247–251, 2012. doi:10.1038/nature11601.

Yamamoto J, Suh J, Takeuchi D, Tonegawa S. Successful execution of working memory linked to synchronized high-frequency gamma oscillations. *Cell* 157: 845–857, 2014. doi:10.1016/j.cell.2014.04.009.

Zandvakili A, Kohn A. Coordinated neuronal activity enhances corticocortical communication. *Neuron* 87: 827–839, 2015. doi:10.1016/j.neuron.2015.07.026.

Zar JH. *Biostatistical Analysis*. Upper Saddle River, NJ: Prentice Hall, 1999.